



Lorentz Factors of Compact Jets in Black Hole X-Ray Binaries

Payaswini Saikia¹, David M. Russell¹, D. M. Bramich^{1,2,3}, James C. A. Miller-Jones⁴ , Maria Cristina Baglio^{1,5} , and Nathalie Degenaar⁶

¹ Center for Astro, Particle, and Planetary Physics, New York University Abu Dhabi, P.O. Box 129188, Abu Dhabi, UAE; ps164@nyu.edu

² Center for Space Science, NYUAD Institute, New York University Abu Dhabi, P.O. Box 129188, Saadiyat Island, Abu Dhabi, UAE

³ Division of Engineering, New York University Abu Dhabi, P.O. Box 129188, Saadiyat Island, Abu Dhabi, UAE

⁴ International Centre for Radio Astronomy Research-Curtin University, GPO Box U1987, Perth, WA 6845, Australia

⁵ INAF, Osservatorio Astronomico di Brera, Via E. Bianchi 46, I-23807 Merate (LC), Italy

⁶ Anton Pannekoek Institute for Astronomy, University of Amsterdam, Postbus 94249, 1090 GE Amsterdam, The Netherlands

Received 2019 June 24; revised 2019 September 22; accepted 2019 September 30; published 2019 December 5

Abstract

Compact, continuously launched jets in black hole X-ray binaries (BHXBs) produce radio to optical/IR synchrotron emission. In most BHXBs, an IR excess (above the disk component) is observed when the jet is present in the hard spectral state. We investigate why some BHXBs have prominent IR excesses and some do not, quantified by the amplitude of the IR quenching or recovery over the transition from/to the hard state. We find that the amplitude of the IR excess can be explained by inclination-dependent beaming of the jet synchrotron emission and the projected area of the accretion disk. Furthermore, we see no correlation between the expected and the observed IR excess for Lorentz factor 1, which is strongly supportive of relativistic beaming of the IR emission, confirming that the IR excess is produced by synchrotron emission in a relativistic outflow. Using the amplitude of the jet fade and recovery over state transitions and the known orbital parameters, we constrain for the first time the bulk Lorentz factor range of compact jets in several BHXBs (with all the well-constrained Lorentz factors lying in the range of $\Gamma = 1.3\text{--}3.5$). Under the assumption that the Lorentz factor distribution of BHXB jets is a power law, we find that $N(\Gamma) \propto \Gamma^{-1.88^{+0.27}_{-0.34}}$. We also find that the very high amplitude IR fade/recovery seen repeatedly in the BHXB GX 339–4 favors a low inclination angle ($\lesssim 15^\circ$) of the jet.

Unified Astronomy Thesaurus concepts: [Stellar mass black holes \(1611\)](#); [High energy astrophysics \(739\)](#); [Jets \(870\)](#); [Black holes \(162\)](#); [Relativistic jets \(1390\)](#); [Infrared astronomy \(786\)](#); [Near infrared astronomy \(1093\)](#); [Infrared excess \(788\)](#)

Supporting material: machine-readable table

1. Introduction

Accreting compact objects on a wide range of physical scales often produce powerful relativistic, collimated outflows known as jets. Astrophysical jets exist in both supermassive and stellar-mass black holes (BHs) and seem to share many common features. Relativistic jets powered by stellar-mass black hole X-ray binaries (BHXBs) typically manifest either as steady, continuous, compact outflows during the hard X-ray state or as discrete, ballistic, superluminous ejections during state transitions (e.g., Fender et al. 2004). The compact jets observed during the hard state of a BHXB are very similar to the relativistic compact jets produced in supermassive BH systems, i.e., active galactic nuclei (AGNs). Both of them share the signature flat-to-inverted ($\alpha > 0\text{--}0.5$, where $F_\nu \propto \nu^\alpha$) radio spectrum, extending up to infrared and sometimes even optical wavelengths. This emission is associated with partially self-absorbed synchrotron radiation originating at a steady, unresolved, compact jet (Blandford & Königl 1979). A tight correlation has been found between near-simultaneous observations of the jet radio luminosity and the X-ray luminosity in BHXBs in the hard state (e.g., Corbel et al. 2003; Gallo et al. 2003, 2014). The same relation also extends to AGNs through the X-ray and optical fundamental plane of BH activity (e.g., Merloni et al. 2003; Falcke et al. 2004; Saikia et al. 2018), suggesting scale invariance of compact, relativistic jets.

The observed luminosity of the jet is affected by relativistic beaming, which depends on the bulk Lorentz factor and the viewing angle, or the inclination of the source. A clear understanding of these intrinsic properties of a jet is crucial for

constraining the physics of the jet-launching region, collimation and acceleration of jets, and the intrinsic physical properties of the BHs. There are many studies that have estimated the bulk Lorentz factor for jets in AGNs and found a parent distribution in the form of a power law (e.g., Padovani & Urry 1992; Lister & Marscher 1997; Kellermann et al. 2004; Jorstad et al. 2005; Saikia et al. 2016). However, the bulk Lorentz factor in BHXB jets is notoriously difficult to measure, with to date only weak constraints for a few BHXBs. While Gallo et al. (2003) used the scatter in the radio/X-ray relation of BHXB jets to constrain the Lorentz factors of compact jets to $\Gamma < 2$, Heinz & Merloni (2004) showed that this correlation does not exclude high values of Lorentz factors. Meanwhile, for transient jets launched during state transitions, Fender (2003) argued that one can only estimate a lower limit on the Lorentz factors by using two-sided jet proper motions. Miller-Jones et al. (2006) used opening angles of transient jets to estimate the bulk Lorentz factor of these sources to have a mean $\Gamma > 10$, assuming that the observed opening angles are due to the transverse Doppler effect.

In this paper, we adopt a simple model to constrain the Lorentz factor of the compact jets in several BHXBs, using IR observations. For some BHXBs, the accretion disk tends to dominate the IR emission throughout the outbursts. However, for many sources (e.g., XTE J1550–564, Jain et al. 2001; 4U 1543–47, Buxton & Bailyn 2004; H1743–322, Chaty et al. 2015; XTE J1650–500, Curran et al. 2012; GX 339–4, Corbel & Fender 2002; Homan et al. 2005), there is an IR excess owing to synchrotron emission produced in the jets.

It has been found that the IR excess above the disk component is prominent in the hard state, with a correlation between IR and X-ray luminosities similar to the radio/X-ray correlation (e.g., Homan et al. 2005; Russell et al. 2006; Coriat et al. 2009; Vincentelli et al. 2018). The IR excess is also absent in the soft state, following the behavior of the radio jet (e.g., Migliari et al. 2007; Kalemci et al. 2013). The IR emission in the soft state is dominated by the accretion disk (e.g., Homan et al. 2005). The IR excess appears to fade and recover close to the transition away from the hard state (Coriat et al. 2009; Cadolle Bel et al. 2011; Baglio et al. 2018), whereas the radio emission can persist over the transitions, existing in the intermediate states (e.g., Fender et al. 2004; Miller-Jones et al. 2012). This was found to be due to an evolving jet spectrum (Corbel et al. 2013; van der Horst et al. 2013; Russell et al. 2014a), whereby the spectral break (between the partially self-absorbed, optically thick synchrotron spectrum and the optically thin spectrum) is correlated with the X-ray hardness over the transition, and this correlation even exists in low-luminosity AGNs (Koljonen et al. 2015). Indeed, the IR excess in the hard state has an optically thin synchrotron spectrum (e.g., Gandhi et al. 2011; Rahoui et al. 2012; Russell et al. 2013a; Baglio et al. 2018), and although alternative inflow models have been proposed for the origin of the IR excess (Poutanen et al. 2014), it has been shown that the general properties are more in line with a jet origin (e.g., Kalemci et al. 2013).

To date, there is no explanation as to why some sources appear to have prominent IR excesses (e.g., GX 339–4; Corbel & Fender 2002; Homan et al. 2005) while others do not (e.g., XTE J1720–318; Chaty & Bessolaz 2006). It has been shown, however, that sources that are IR-faint on the IR/X-ray correlation are also radio-faint on the radio/X-ray correlation (Curran et al. 2012; Russell et al. 2013a; Chaty et al. 2015). Since the jets are relativistic, we expect the IR emission to be Doppler boosted, i.e., beamed toward or away from the observer. Therefore, sources with jets pointing toward our line of sight may have more prominent IR excesses than those directed away. If the jet axis is perpendicular to the orbital plane (see discussion below), then one can test for a correlation between the inclination angle and the jet emission using measured inclination angles. This was recently tested by Motta et al. (2018) using radio data—they found that sources with low inclination angles appear, in most cases, to be radio-loud on the radio/X-ray correlation, whereas higher-inclination sources tended to be radio-quiet. The IR excess will also be affected by the emission from the accretion disk. Larger disks and face-on disks (low inclination) will tend to decrease the jet/disk emission ratio. For neutron star X-ray binaries, which also have IR excesses in some cases, it was suggested that systems with small disks have more prominent IR excesses (Russell et al. 2007).

Here we explore whether relativistic beaming and relative disk emission can explain the observed IR excess in BHXBs as measured from the amplitude of the IR fade and recovery over state transitions. We describe our sample of BHXBs in Section 2 and gather from the literature the physical properties of the sources, as well as infrared data during outbursts. In Section 3 we discuss the model and the methods used to estimate the expected IR flux excess in these sources from their observed parameters, such as the masses involved, orbital period, and inclination angle. In Section 4 we present the Bayesian framework used to constrain the jet Lorentz factors

for our sample of BHXBs. Finally, in Section 5 we discuss the results of the paper, as well as caveats involved in our method, and compare our findings with previous literature.

2. Sample

About 77 BHXBs are known in the Galaxy (though only 21 of these are dynamically confirmed as hosting BHs; Tetarenko et al. 2016). We have compiled a list of 14 BHXBs for which reliable IR excess information is available in the literature. In this section, we describe the methods used to estimate the IR excess and inclination angles. We also present the sources and caveats of the infrared observations and discuss the BH properties used in this study.

Methods of estimating IR excess: We use three methods to measure the IR excess over disk emission. When well-sampled near-infrared (NIR) K -band (or H -band) light curves are available, we estimate the amplitude of the IR excess by simply measuring the magnitude change observed over the transition. This transition usually occurs fairly quickly, with a clear IR fade or rise lasting days to a week or so, whereas the outer disk component in the IR is largely unchanged over this short period of time. Hence, this method provides a good measure of the IR jet quenching and recovery (e.g., Buxton & Bailyn 2004; Russell et al. 2010, 2012). For sources that do not make state transitions (e.g., sources that remain in the hard state), we estimate the amplitude of the IR excess above the disk component from published optical–IR spectral energy distributions (SEDs), where the disk and jet components are both measured. Finally, in one case, H1743–322, we infer the IR excess amplitude from the change in the IR J – K_s color between hard-state and soft-state observations (see Section 2.5 for details).

In order to estimate the contribution of the companion star to the total IR flux, we compare the companion’s quiescence IR flux to the observed flux of the system in all cases. We find that in only 1 source, GRO J1655–40, the companion flux exceeds 10% of the observed flux and hence needs to be taken care of (see Section 2.7 for details). For all the other sources in our sample, we find that the IR contribution of the companion is much less than 10% of the total IR flux of the system.

We chose to use the IR flux change as a ratio (flux with jet on/flux with jet off) rather than an absolute flux value. We do this to be able to compare between sources, because the flux values depend on the distance, whereas the ratio does not. Distances are highly uncertain in many cases. This is also one of the reasons why we have chosen not to use radio data in this work. The disk does not contribute to the radio emission, and the nonjet radio emission in the soft state is approximately zero. We therefore could not use a jet on/off flux ratio if we were to use radio data, and we would be forced to use the absolute flux values, requiring the distance, which introduces errors. In addition, radio data over the state transition are complicated by bright transient ejections, and monitoring of the compact, flat-spectrum jet over the transitions is poorly sampled in many cases. In a future study, radio data could be used for sources with well-known distances and well-sampled light curves, to infer the bulk Lorentz factors of jets at (radio-emitting) large distances from the BH. By using IR data here, we are probing the Lorentz factor of jets close to their launching region (at distances on the order of ~ 0.1 lt-s from the BH; Gandhi et al. 2017).

Methods of deciding inclination constraints: At present, there are mainly three ways to estimate the inclination angle of

a BHXB: (i) using the orbital inclination of the companion star to our line of sight as typically measured from ellipsoidal modulation of the companion light curve in quiescence, (ii) using the inclination of the inner disk close to the central BH as typically measured from X-ray spectral fitting, and (iii) using the inclination of the jets as measured from the relative fluxes and sizes of the two jets estimated from radio observations. We have chosen to exclude inclinations constrained via X-ray spectral fitting because they are highly model dependent and can give wildly differing values depending on the assumptions and models used (see, e.g., Hiemstra et al. 2009). Moreover, there is increasing evidence that at least in some sources the inner disk is precessing (see, e.g., Ogilvie & Dubus 2001; Liska et al. 2018; Motta et al. 2018; Miller-Jones et al. 2019), and perhaps that causes (some of) the discrepancy between inclinations measured through X-ray reflection models. On the other hand, the discrepancy in inclinations estimated from optical measurements is usually only a few degrees (Kreidberg et al. 2012). For uniform selection and reliable measurement of inclination, we only consider inclinations derived either from optical measurements or through radio observations when optical measurements are unavailable.

2.1. XTE J1118+480

XTE J1118+480 was discovered by the All Sky Monitor (ASM) on the *RXTE* (*Rossi X-ray Timing Explorer*) satellite in 2000 by Remillard et al. (2000). The inclination measurements reported by different studies all lie in the range 68° – 82° (e.g., McClintock et al. 2001; Wagner et al. 2001; Zurita et al. 2002; Kreidberg et al. 2012). Tetarenko et al. (2016) established a comprehensive database of BHXBs named the Whole-sky Alberta Time-resolved Comprehensive black-Hole Database Of the Galaxy (WATCHDOG), where they calculated a central BH mass of $7.30 \pm 0.73 M_\odot$ and tabulated a distance of 1.7 ± 0.1 kpc (Gelino et al. 2006), a mass ratio between the companion star and the central BH of 0.024 ± 0.009 (Calvelo et al. 2009), and an orbital period of 4.078414 ± 0.000005 hr (Torres et al. 2004).

Hynes et al. (2003, 2006) observed this source in the IR band, but because it remained in the hard state throughout both its outbursts, it is difficult to separate out the disk and jet components. McClintock et al. (2001) modeled the optical/UV with a multitemperature disk and found that the NIR-band fluxes needed to be multiplied by 0.8 to lie on the extrapolation of the optical disk spectrum. So the jet component “factor flux drop” can be estimated as $1/0.8 = 1.25$, which is a change of ~ 0.24 mag. However, Chaty et al. (2003) modeled the broadband SED of the source and found the *K*-band flux to be 1.24 orders of magnitude brighter than the disk component. Therefore, the jet component “factor flux drop” can be estimated as $10^{1.24} \approx 17.33$, which is a change of ~ 3.10 mag. Clearly the jet contribution is model dependent, and hence we use a range of IR excess to incorporate both the values in our final analysis to estimate the Lorentz factor.

2.2. Swift J1357.2–0933

Swift J1357.2–0933 was detected in 2011 by the *Swift* Burst Alert Telescope (Krimm et al. 2011). Corral-Santana et al. (2013) performed time-resolved optical spectroscopy of broad, double-peaked $H\alpha$ emission in this BHXB and estimated an orbital period of 2.8 ± 0.3 hr. Mata Sanchez et al. (2015) studied

this source during quiescence and estimated a massive BH with $M_{\text{BH}} > 9.3 M_\odot$, a companion star with mass $\sim 0.4 M_\odot$ (we conservatively assume an error of 50%, i.e., $M_{\text{CS}} = 0.4 \pm 0.2 M_\odot$), and a very high orbital inclination ($i > 80^\circ$). The distance to the source ranges from ~ 1.5 to 6.3 kpc (Rau et al. 2011; Shahbaz et al. 2013).

Shahbaz et al. (2013) performed high time resolution ULTRACAM optical and NOTCam infrared observations of Swift J1357.2–0933 during the 2011 outburst. They showed that during the 2011 outburst the *K*-band flux was $\sim 0.4 \pm 0.05$ dex brighter than the disk model that was well fit to the SED. This is a factor of 2.51 ± 1.12 flux change, or a 1.00 ± 0.13 mag change.

2.3. MAXI J1535–571

MAXI J1535–571 was discovered by MAXI in 2017 (Negoro et al. 2017). Shang et al. (2019) performed X-ray spectral analysis of the source and estimated the mass of the BH to be in the range of 7.7 – $10.0 M_\odot$. The inclination of the source is not properly constrained, with reports of estimated measurements from model-dependent X-ray spectral fitting ranging from 27° to 67° (e.g., Gendreau et al. 2017; Stiele & Kong 2018; Xu et al. 2018). As different values of inclinations for this source in the literature are all from X-ray measurements and they are in disagreement with each other by more than 30° , we consider the inclination of this source to be very uncertain, and we do not use it for our study.

The NIR (*JHK*) and optical (*yzir*) light curves of MAXI J1535–571 during its 2017/2018 outburst are reported in Baglio et al. (2018). A clear fading is observed over the hard-to-soft transition, with the drop in flux being more significant toward the lowest frequencies. The magnitude drop measured from the light curve is 2.10 ± 0.16 mag in the *K* band.

2.4. 4U 1543–47

4U 1543–47 is a recurrent X-ray transient first discovered in 1971 (Matilsky et al. 1972). Orosz et al. (1998) performed spectroscopic observations of the source and found the distance to the source to be $\sim 9.1 \pm 1.1$ kpc, assuming the secondary to be on the main sequence. The inclination of the source was found to be $20.7^\circ \pm 1.5^\circ$ (Orosz 2003). Russell et al. (2006) compiled from the literature a central BH mass of $9.4 \pm 1.0 M_\odot$ and a companion mass of $2.45 \pm 0.15 M_\odot$. The orbital period of the source is 26.79377 ± 0.00007 hr (Orosz 2003).

Buxton & Bailyn (2004) studied rebrightening of the *K*-band light curve and reported a *K*-band magnitude change from 14.06 ± 0.03 mag on MJD 52,473.221100 to a value of 12.19 ± 0.01 mag on MJD 52,487.961500. This implies a change of 1.87 ± 0.03 mag during state transition.

2.5. XTE J1550–564

XTE J1550–564 was discovered by *RXTE*/ASM (Smith et al. 1998). Orosz et al. (2011) used moderate-resolution optical spectroscopy and NIR photometry of the source to find an orbital period of 1.5420333 ± 0.0000024 days ($37.008799 \pm 5.8 \times 10^{-5}$ hr). Using the light curves obtained, they estimated an inclination range of 57.7° – 77.1° , a BH mass of $9.10 \pm 0.61 M_\odot$, a secondary-star mass of $0.30 \pm 0.07 M_\odot$, and a distance of $4.38^{+0.58}_{-0.41}$ kpc.

H-band light curves of XTE J1550–564 were reported by Jain et al. (2001) and also analyzed in Russell et al.

(2007, 2010, 2011). These observations showed that during the hard-to-soft transition the H band faded from 13.3815 ± 0.0225 mag to 14.3365 ± 0.0645 mag (i.e., a change of 0.955 ± 0.068 mag). The soft-to-hard transition showed an H -band rise from 14.8770 ± 0.0750 mag to 13.8905 ± 0.0135 mag (i.e., a change of 0.987 ± 0.076 mag). For this analysis, we use the combined (averaged) value of $\sim 0.97 \pm 0.07$ mag change.

2.6. XTE 1650–500

XTE J1650–500 was discovered in 2001 September by the *RXTE*/ASM (Remillard 2001). Orosz et al. (2014) used optical observations to derive an orbital period of 0.3205 ± 0.0007 days ($\sim 7.69 \pm 0.02$ hr) and estimated the upper-limit mass of the central BH to be $7.3 M_{\odot}$. Kreidberg et al. (2012) estimated an inclination of $i = 75.2 \pm 5.9$. Tetarenko et al. (2016) calculated a central BH mass of $4.72 \pm 2.16 M_{\odot}$, estimated a mass ratio between the companion star and the central BH in the range of 0.0–0.5, and tabulated a distance of 2.6 ± 0.7 kpc (Homan et al. 2006).

Curran et al. (2012) showed that there is a clear IR drop over the hard-to-soft transition. There is no light curve of the drop itself, but it fades from $K_s = 13.29 \pm 0.13$ on MJD 52,161.03691 to $K_s = 13.82 \pm 0.12$ on MJD 52,177.00145, showing an IR drop of 0.53 ± 0.18 mag over the transition. It is important to note that there is only one data point in the hard state. However, the hard state point is just before (within a day) the hard-to-intermediate state transition when the IR starts to fade in all sources with a well-sampled light curve. So the drop of 0.53 ± 0.18 mag is likely to be accurate within errors.

2.7. GRO J1655–40

GRO J1655–40 was discovered in 1994 by BATSE on board CGRO (Harmon et al. 1995). Hjellming & Rupen (1995) estimated the distance to the system to be 3.2 ± 0.5 kpc. Greene et al. (2001) performed *BVIJK* photometry of the source during full quiescence and found an orbital period of 2.62191 ± 0.00020 days (or 62.9258 ± 0.0048 hr), an inclination angle of 70.2 ± 1.9 , and a BH mass of $6.3 \pm 0.5 M_{\odot}$. Later, Beer & Podsiadlowski (2002) estimated the mass of the BH to be $5.4 \pm 0.3 M_{\odot}$ and the mass of the companion star to be $1.45 \pm 0.35 M_{\odot}$.

From Kalemci et al. (2016), we estimate the hard-to-intermediate state transition to have happened around MJD 53,435 during its 2005 outburst. Shidatsu et al. (2016) and Kalemci et al. (2016) showed no visible change in K band at this time, with flux changing by a factor of less than 1.25 (0.24 mag).

One peculiar thing about GRO J1655–40 is that unlike the other sources in our sample, the contribution of the companion star to the IR flux of the system is more than 10%. From Kalemci et al. (2016), the average magnitude of the system in the 5 days preceding the transition is 12.222 ± 0.029 mag ($F_1 = 8.616$ mJy). The average magnitude of the system 5 days after the transition (including the transition day) is 12.228 ± 0.059 mag ($F_2 = 8.569$ mJy). The K -band magnitude of the system during quiescence is 13.3 mag ($F_Q = 3.193$ mJy). So the companion star produces $\sim 37\%$ of the flux in this system at the time of the transition. Removing the IR flux contribution of the companion star (which is constant over the transition), we find that the flux ratio becomes $(F_1 - F_Q)/(F_2 - F_Q) = 1.009$. This corresponds to a magnitude change of ~ 0.01 mag, which is

Table 1
IR Excess Measured in Different State Transitions of GX 339–4 during 2002–2011

Year	MJD During Transition	IR mag Change
2002 (rise)	2390.7649–2405.8173	3.11 ± 0.028
2003 (fade)	2738.82521–2759.83738	1.51 ± 0.036
2004 (rise)	3217.6421–3231.62454	1.56 ± 0.028
2005 (fade)	3476.84335–3491.85172	1.65 ± 0.036
2007 (rise)	4134.86885–4147.84173	3.20 ± 0.028
2007 (fade)	4239.80197–4254.79423	1.50 ± 0.036
2010 (rise)	5293.8583–5302.8286	2.98 ± 0.036
2011 (fade)	5605.88975–5617.77736	1.64 ± 0.036

Note. IR rise is measured during the transition toward the hard state, while a fade is observed during the transition away from the hard state.

much smaller than the IR flux change limits (0–0.24 mag) we have used in the above analysis. We therefore adopt the more conservative range, 0–0.24 mag, as the minimum and maximum flux drop over the transition.

2.8. GX 339–4

GX 339–4 was discovered in 1972 by the MIT X-ray detector on board the *Orbiting Solar Observatory 7* (*OSO 7*) satellite. It shows relatively frequent outburst cycles of various strengths (typically once every 2–3 yr). The orbital period of the system is estimated to be 1.7557 ± 0.0004 days ($\sim 42.14 \pm 0.01$ hr) by measuring Doppler shifts of fluorescent lines (Hynes et al. 2003). The distance to the source is expected to be in the range of 6–15 kpc (Hynes et al. 2004). However, the mass of the compact object and companion star and the inclination of the system are very weakly constrained. Heida et al. (2017) analyzed the radial velocity curve and projected rotational velocity of the donor to set limits of $2.3 M_{\odot} \leq M_{\text{BH}} \leq 9.5 M_{\odot}$ to the accretor mass and a mass ratio $q = 0.18 \pm 0.05$. The inclination angle of GX 339–4 is not well constrained, and values in the literature range from $13^\circ \pm 3^\circ$ (Miller et al. 2004, from X-ray) and 0° – 30° (Wu et al. 2001, from optical) to $50^\circ \pm 10^\circ$ (Basak & Zdziarski 2016, from X-ray) and 57.5 ± 20.5 (Heida et al. 2017, from optical). Owing to the high uncertainty in the inclination angle, we do not include this source in our final analysis.

GX 339–4 has a good coverage of IR excess measured during different transitions over the years (see Table 1) owing to intensive monitoring by SMARTS (Coriat et al. 2009; Buxton et al. 2012; Dincer et al. 2012). All the IR excess magnitudes reported for GX 339–4 are roughly in two different ranges, 1.50–1.65 mag and 2.98–3.20 mag. We discuss the possible reasons behind these two observed IR excess values, any relation of the differences with the type of transition, and their correlation with the X-ray luminosity in the discussion section.

2.9. H1743–322

H1743–322 was discovered during an outburst in 1997 by the *Ariel V* satellite (Kaluzienski & Holt 1977) and *HEAO-1* satellite (Doxsey et al. 1977). Steiner et al. (2012) used a kinematic model of the jets to estimate the distance to this source as 8.5 ± 0.8 kpc and the inclination angle of the jets as $75^\circ \pm 3^\circ$. In the literature, there is no inclination measurement using optical data. Currently, the BH mass, companion star mass, and orbital period of this system are also not clearly known.

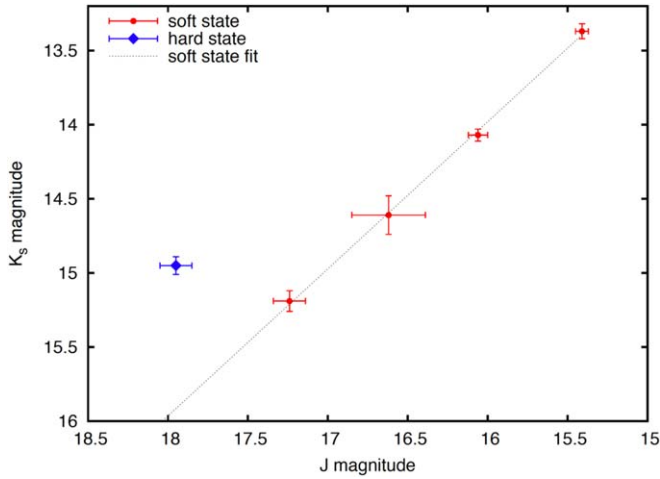


Figure 1. IR observation of H1743 during soft (red) and hard (blue) states from Chaty et al. (2015) (see text for explanation).

A direct measurement of the IR excess from the light curve is not available for this source because its outbursts were only partly sampled in the IR. However, Chaty et al. (2015) published IR magnitudes of the source from several outbursts. We find that there is a strong correlation between the J - and K_S -band magnitudes in the soft state (see Figure 1), which is very likely due to disk emission. In the hard state (when we expect a jet contribution), the data deviate from the correlation, the K_S band being brighter than expected from the relation, by 0.97 ± 0.12 mag. This is therefore a measure of the K_S -band excess due to the jet emission, above the disk component, so we take this as the magnitude change over the state transition.

2.10. XTE J1752–223

XTE J1752–223 was discovered in 2009 by *RXTE* (Markwardt et al. 2009). Shaposhnikov et al. (2010) used correlations between spectral and variability properties with GRO J1655–40 and XTE J1550–564 and estimated a distance of 3.5 ± 0.4 kpc and a BH mass of $9.6 \pm 0.9 M_\odot$. Russell et al. (2012) performed optical monitoring of this source during its 2009–2010 outburst and decay to quiescence and estimated a likely orbital period of <22 hr. Miller-Jones et al. (2011) measured the inclination angle of the source to be $<49^\circ$.

Chun et al. (2013) performed simultaneous X-ray and optical/NIR observations of the source during its outburst decay in 2010. They showed that over the transition from the soft state toward the hard state, the H -band emission increased by a small amount: 0.35 ± 0.18 mag.

2.11. Swift J1753.5–0127

Swift J1753.5–0127 was discovered in outburst by *Swift*/BAT in 2005 (Palmer et al. 2005). It had a ~ 12 yr long outburst, with a mini-outburst toward the end (Plotkin et al. 2016; Shaw et al. 2019). Zurita et al. (2008) estimated the photometric orbital period of the source to be 3.2443 ± 0.0010 hr. Later, Neustroev et al. (2014) used radial velocity measurements to estimate an orbital period of 2.85 ± 0.01 hr, which is one of the shortest orbital periods of any known BHXB. For our calculation, we use an orbital period range of 2.85–3.24 hr to incorporate both values. Using high-resolution, time-resolved optical spectroscopy, Shaw et al. (2016b) estimated the mass of

the compact object to be $>7.4 \pm 1.2 M_\odot$. Although the mass of the companion star is not known, Neustroev et al. (2014) estimated it to be in the range of 0.17 – $0.25 M_\odot$ using empirical and theoretical mass–period relations for a 2.85 hr orbital period binary. The inclination of the source is not precisely known; while Neustroev et al. (2014) suggest a lower limit of 40° , Shaw et al. (2019) predict an upper limit of 80° . The distance to this source is also not well constrained, and different studies report a large range of possible distances of 1–10 kpc (Cadolle Bel et al. 2007; Zurita et al. 2008; Froning et al. 2014).

Tomsick et al. (2015) carried out a multiwavelength campaign of Swift J1753.5–0127 in the hard state during 2014 April. The K -band flux was measured as ~ 0.4 – 0.7 mJy, while the jet emission was ~ 0.08 mJy (estimated from Figure 8(b) of Tomsick et al. 2015). Using these estimates, we can assume a factor change in the range of 1.13–1.25 when the jet switches off, although we cannot rule out the possibility that the jet could be a lot fainter. In Rahoui et al. (2015), the K -band flux is calculated to be ~ 0.7 mJy and the disk emission is measured as ~ 0.3 mJy. So if the jet would switch off, a factor change of 1.75 would be expected. Based on these two studies, we can safely assume a factor flux change in the range of 1–1.75 (equivalently 0–0.6 mag).

2.12. MAXI J1836–194

MAXI J1836–194 was discovered in the early stages of its outburst in 2011 (Negoro et al. 2011). Russell et al. (2014b) studied the Very Large Telescope optical spectra of the source and estimated an inclination angle between 4° and 15° , assuming distances between 4 and 10 kpc. The donor is expected to be a main-sequence star with a mass of $<0.65 M_\odot$ and with an orbital period of <4.9 hr. The mass of the compact object is not well constrained. However, we can estimate a lower limit of $2 M_\odot$, given the lower limit on the distance of 4 kpc.

Data from Russell et al. (2013b, 2014b) showed that there is an IR magnitude change during state transition from 13.86 ± 0.37 mag on MJD 55,820.12 to 11.48 ± 0.21 mag on MJD 55,845.0511. This shows a rise of IR emission by 2.38 ± 0.43 mag in ~ 24.9 days.

2.13. XTE J1859+226

XTE J1859+226 was first detected by *RXTE* in 1999 (Wood et al. 1999). Corral-Santana et al. (2011) used both optical photometry and spectroscopy to find an orbital period of 6.58 ± 0.05 hr and an inclination angle of $60^\circ \pm 3^\circ$. Tetarenko et al. (2016) have tabulated a central BH mass of $10.83 \pm 4.67 M_\odot$ and a companion-star upper-limit mass of $<5.41 M_\odot$. The distance to this source is still not certain, with different studies inferring statistically different distances, for example, 11 kpc (Zurita et al. 2002), 4.6–8.0 kpc (Hynes et al. 2000), and 8 ± 3 kpc (Hynes 2005). We adopt the latter for our calculation, as it encompasses all the values reported.

Hynes et al. (2002) observed the source in J , H , and K bands during 1999–2000 and showed that there is a small IR excess in the lowest frequencies, at the beginning of the state transition from the hard state to the soft state. As shown in Brocksopp et al. (2002), the initial hard state is until MJD $\sim 51,464$, after which the source made the transition. The first NIR data in Hynes et al. (2002) are on MJD 51,465, at the start of the transition. The K -band NIR excess can be seen in the first SED

Table 2

Physical Properties and Orbital Parameters Obtained from the Literature, for All the BHXBs That Have Previous Measurements/Estimates of Infrared Excess Observed during State Transitions

Name	Inclination (deg)	$M_{\text{BH}} (M_{\odot})$	$M_{\text{CS}} (M_{\odot})$	$P_{\text{orb}} (\text{hr})$	Distance (kpc)	IR Excess (mag)	IR
XTE J1118+480	68–82	7.3 ± 0.7	0.18 ± 0.07	$4.078414 \pm 5 \times 10^{-6}$	1.7 ± 0.1	0.24–3.10*	<i>K</i>
Swift J1357.2–0933	80–90	>9.3	0.4 ± 0.2	2.8 ± 0.3	1.5–6.3	1.00 ± 0.13	<i>K</i>
<i>MAXI J1535–571</i>	...	7.7–10.0	2.10 ± 0.16	<i>K</i>
4U 1543–47	20.7 ± 1.5	9.4 ± 1.0	2.45 ± 0.15	$26.79377 \pm 7 \times 10^{-5}$	9.1 ± 1.1	1.87 ± 0.03	<i>K</i>
XTE J1550–564	57.7–77.1	9.1 ± 0.6	0.30 ± 0.07	$37.008799 \pm 5.8 \times 10^{-5}$	$4.38^{+0.58}_{-0.41}$	0.97 ± 0.07	<i>H</i>
XTE J1650–500	75.2 ± 5.9	4.7 ± 2.2	<2.36	7.69 ± 0.02	2.6 ± 0.7	0.53 ± 0.18	<i>K</i>
GRO J1655–40	70.2 ± 1.9	5.4 ± 0.3	1.45 ± 0.35	$62.9258 \pm 4.8 \times 10^{-3}$	3.2 ± 0.5	0.00–0.24	<i>K</i>
<i>GX 339–4</i>	0–78	2.3–9.5	0.41–1.71	42.14 ± 0.01	6–15	1.50–3.20 ⁺	<i>H</i>
<i>H1743–322</i>	75 ± 3	8.5 ± 0.8	0.97 ± 0.12	<i>K</i>
<i>XTE J1752–223</i>	<49	9.6 ± 0.9	...	<22	3.5 ± 0.4	0.35 ± 0.18	<i>H</i>
Swift J1753.5–0127	40–80	>7.4	0.17–0.25	2.85–3.24	1–10	0.0–0.6	<i>K</i>
<i>MAXI J1836–194</i>	4–15	>2.0	<0.65	<4.9	4–10	2.38 ± 0.43	<i>K</i>
XTE J1859+226	60 ± 3	10.8 ± 4.7	<5.41	6.58 ± 0.05	8 ± 3	0.68 ± 0.03	<i>K</i>
<i>Swift J1910.2–0546</i>	...	>2.9	...	2.2–4.0	>1.70	0.41 ± 0.28	<i>K</i>

Note. The columns include the name of the source, inclination angle, mass of the BH, mass of the companion star, orbital period, distance, IR excess, and the IR band in which the excess has been measured, respectively. For each of the sources, the values obtained from the literature and their references are discussed in the text. We do not include the sources in italics in our Bayesian analysis because their parameters are not well measured; however, we include them in the table for completeness and potential future studies. Values in the table have been rounded to a uniform level of precision. Ellipses: no measurement is available; asterisk: model-dependent values of IR excess explained in the text, plus sign: many measurements available in the literature are explained properly in Table 1.

on MJD 51,465, where the *J*-band data point is close to the disk spectrum (see Figure 4; Hynes et al. 2002). Comparing that with the SED obtained on MJD 51,469, when the *K*-band lies on the disk extrapolation from optical/UV, we can say that the jet has faded while the disk remained. The *K*-band drop during this period is calculated as 0.68 ± 0.03 mag.

2.14. Swift J1910.2–0546

Swift J1910.2–0546 was simultaneously discovered by *Swift*/BAT (Krimm et al. 2012) and MAXI (Usui et al. 2012) in 2012. Lloyd et al. (2012) and Casares et al. (2012) examined periodic variations in the optical light curve to estimate the orbital period to be ~ 2.2 and ~ 4 hr, respectively. Nakahira et al. (2012) did long-term monitoring of the source and put a lower limit on the mass of the compact object of $>2.9 M_{\odot}$ and on the distance of >1.70 kpc. The inclination angle is estimated to be between 4° and 22° from X-ray spectral fitting (Reis et al. 2013). No optical measurements of the inclination have been reported; hence, we do not use it in our calculations.

Degenaar et al. (2014) monitored the evolution of this source during outburst for 3 months at different wavelengths and showed that the transition from the hard state to the soft state is around day 103 (i.e., \sim MJD 56,180; see Figure 2 of Degenaar et al. 2014). Multiwavelength light curves and color evolution (see Figure 3 of Degenaar et al. 2014) showed an unusual drop followed by a rise in all bands just before this state transition, with no color change. So the flux drop we calculate is after that, between day 103 and day 109 (MJD 56,180–56,186), when the color change occurred, indicating a decrease in jet emission. We find that the IR emission drop over the hard-to-soft transition is 0.41 ± 0.28 mag.

Final sample: Our final sample consists of only those nine sources for which we have reliable constraints for all of the required parameters. We remove H1743–322 from our analysis, as the masses and the orbital period are not known for this source (although it is included in Figure 3). We exclude XTE J1752–223 from our final sample, as it has only upper limits for

both the inclination angle and the orbital period, while the mass of the companion star is completely unknown. We also remove Swift J1910.2–0546 and MAXI J1535–571, as no optical and radio measurements of the inclination have been reported in the literature. And finally, as there are various model-dependent values of the inclinations reported for GX 339–4 in the literature (with inclination values in disagreement with each other by more than 30°), we also exclude this source from our analysis, although we discuss GX 339–4 later in more detail. In Table 2, we list all of the BHXBs with measured IR excess, and we identify the excluded sources in italics.

3. MODEL

3.1. Qualitative Theoretical Prediction

Theoretically, the jet luminosity should correlate with the inclination angle if the emission is subject to relativistic beaming. Indeed, it has been shown that some of the sources with the brightest IR excesses compared to their disks are systems with a low inclination angle (e.g., 4U 1543–47 and MAXI J1836–194; see Table 2 and Figure 3).

For high-inclination systems, the disk is almost edge-on, which reduces the disk emission but not the jet emission (if the jet is not highly beamed). This can lead to relatively bright IR excesses in high-inclination systems. For intermediate inclination angles ($\sim 30^{\circ}$ – 60°), no bright IR excess is expected for any Lorentz factor, and indeed all of the BHXBs with inclination angles within this range do not have prominent IR excesses (see Figure 3). When the inclination is low, the jet is oriented directly toward the line of sight, and a prominent IR excess is expected owing to relativistic beaming (see Figure 2).

3.2. Model Prediction of the IR Excess

When a BHXB is in the soft state, the jet is quenched, and hence any NIR flux observed can be assumed to originate from the accretion disk. When the source transits to the hard state, the jet reappears and we see an excess of flux in the NIR

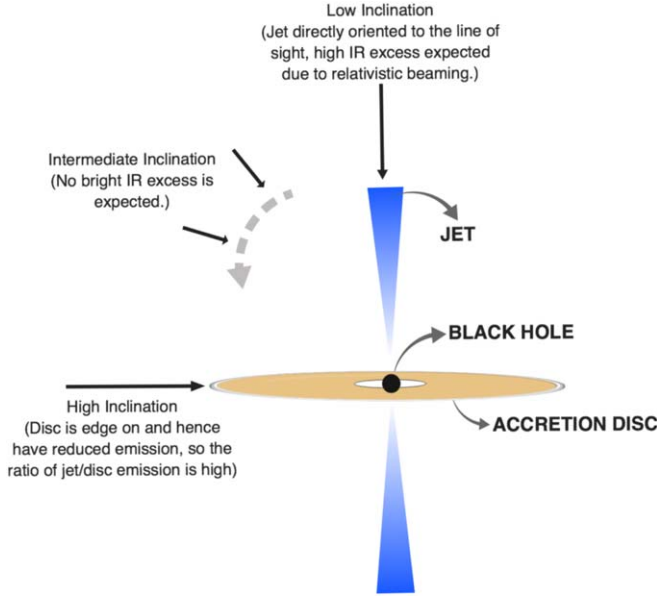


Figure 2. Schematic diagram to qualitatively explain the expected IR excess observed for different BHXB sources, depending on their inclinations.

wavelength range. If the appearance/disappearance of the NIR excess observed in BHXBs during state transition is occurring because the jet switches on/off, then we can use a simple analytical model to predict the relative flux excess expected for each source. To do this, we calculate the projected area of the accretion disk (to estimate the relative disk emission) and the Doppler beaming as a function of the Lorentz factor (to infer the jet emission).

The projected area of the accretion disk is calculated depending on the size of the disk and the inclination angle i . Assuming that the disk is irradiated by a point source, the disk reprocessing scales as $R^{2/7}$, where R is the radius of the outer disk (see the discussion along with Equations (5.94) and (5.95) in Frank et al. 2002 and references therein). Hence, projected (observed) disk reprocessing is $\propto R^{2/7} \cos(i)$, where R is proportional to the orbital separation, and the orbital separation is proportional to $(M_{\text{BH}} + M_{\text{CS}})^{1/3} P_{\text{orb}}^{2/3}$ (e.g., van Paradijs & McClintock 1994; Russell et al. 2006). Hence, the projected (observed) disk reprocessing obeys

$$D_{\text{pr}} \propto (M_{\text{BH}} + M_{\text{CS}})^{2/21} P_{\text{orb}}^{4/21} \cos(i). \quad (1)$$

Hence, the IR disk emission is $F_{\text{disk}} = k_1 D_{\text{pr}}$, where k_1 is an unknown constant that depends on, e.g., the disk reprocessing efficiency.

The Doppler factor for jet emission Δ_{jet} represents the observed radio luminosity of the jet relative to its intrinsic (rest-frame) radio luminosity. This relation can be described as $S_{\text{jet,obs}} = \Delta_{\text{jet}} \times S_{\text{jet,intr}}$. Δ_{jet} is calculated following the same method as in Gallo et al. (2003) via

$$\Delta_{\text{jet}} = \frac{(\delta_{\text{rec}})^2 + (\delta_{\text{app}})^2}{2}, \quad (2)$$

where the receding and approaching factors $\delta_{\text{rec/app}} = \Gamma^{-1} (1 \pm \beta \cos i)^{-1}$; $\beta = v/c$ is the bulk velocity of the radio-emitting material relative to the speed of light, and $\Gamma = (1 - \beta^2)^{-1/2}$ is the corresponding bulk Lorentz factor.

In the soft state, when we do not expect a jet, the IR emission should entirely consist of the disk emission (proportional to

D_{pr}). On the other hand, both the disk and the jet should contribute toward the IR emission in the hard state (where the excess IR flux is proportional to Δ_{jet} ; $F_{\text{jet}} = k_2 \Delta_{\text{jet}}$). Hence, for each of the sources, we can use the calculated projected area of the disk and the Doppler factor of the jet to estimate the predicted magnitude change $\Delta m_{\text{IR,pred}}$ that we expect over state transition. This quantity is obtained via

$$\Delta m_{\text{IR,pred}} = 2.5 \log_{10} \left[\frac{k_1 D_{\text{pr}} + k_2 \Delta_{\text{jet}}}{k_1 D_{\text{pr}}} \right] \quad (3)$$

$$= 2.5 \log_{10} \left[1 + C \frac{\Delta_{\text{jet}}}{D_{\text{pr}}} \right], \quad (4)$$

where $C = k_2/k_1$ is the ratio of the two unknown constants and depends on the disk and jet radiative efficiencies. In our model, we are essentially testing whether the disk size and inclination angle can be used to predict the jet/disk flux ratio in the hard state. For a source at a given disk size and inclination angle, we can predict the jet/disk flux ratio. This requires C to have the same value for all sources. Theoretically, it is known for reprocessing of the disk that the optical luminosity (and hence also the IR luminosity; see Russell et al. 2006) is proportional to the X-ray luminosity as $L_{\text{Opt}} \propto L_{\text{IR}} \propto L_X^{0.5}$ (van Paradijs & McClintock 1994). So we expect the relation $k_1 \propto L_X^{0.5}$. For the jet in the hard state, assuming a flat spectrum from radio to IR wavelengths, and using the fundamental plane, we get $L_R \propto L_{\text{IR}} \propto L_X^{0.7}$. Hence, we can assume $k_2 \propto L_X^{0.7}$ and roughly $C = k_2/k_1 \propto L_X^{0.2}$. Therefore, C can be considered roughly constant and to be having a very weak dependency on both the X-ray luminosity and mass accretion rate. Many observational studies have also confirmed the expected theoretical correlations, mostly following the relation $L_{\text{Opt/IR}} \propto L_X^{0.6}$ (e.g., Homan et al. 2005; Coriat et al. 2009; Bernardini et al. 2016; Vincentelli et al. 2018). So the dependency of the constant C on L_X is even shallower ($C \propto L_X^{0.1}$) when using the observational relations.

Although there are caveats in this assumption, we do not think they should change the dependency much. One caveat is the observed jet break in the spectrum that is often seen in the IR band, which mostly lies in the optically thin part of the synchrotron spectrum. If the jet break frequency also scales with the X-ray luminosity, then the jet IR emission will no longer be proportional to the jet radio emission. But as shown in Russell et al. (2013a), there appears to be no strong relation between the jet break frequency and L_X in the hard state. Hence, we can expect L_R to be proportional to L_{IR} , which is also seen observationally in Russell et al. (2006). Another caveat is that the relation $L_R \propto L_X^{0.7}$ does not hold observationally in all BHXBs. The radio-faint sources seem to have a shallower relation at low L_X and a steeper relation at high L_X . However, it has been found that the radio-faint sources are also IR-faint, so $L_R \propto L_{\text{IR}}$ from the jet should still hold. So we do not expect these caveats to significantly change the assumption of weak dependency of the constant C on L_X and mass accretion rate. In any case, it is important to note that if other parameters play a role, such as different reprocessing efficiencies in different disks, or different jet properties resulting in different jet fluxes for the same inclination and Lorentz factor, then we expect our model to provide a poor description of the data.

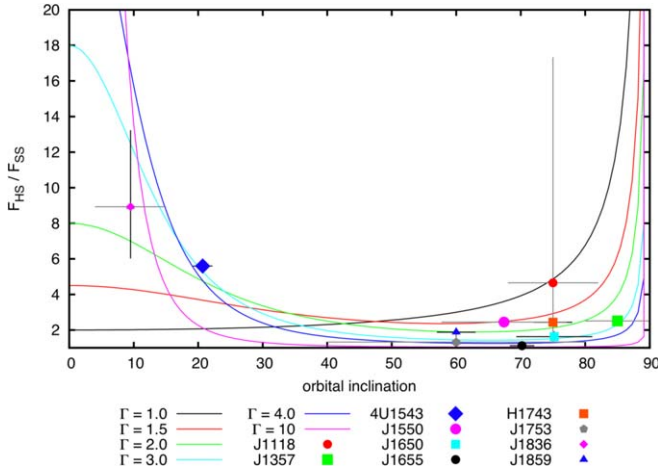


Figure 3. The different lines show the flux change when the jet switches on and off (shown as a ratio of IR emission in the hard state vs. the soft state), vs. the orbital inclination for different Lorentz factors. The points with error bars include all the BHXBs with well-constrained measurements of inclination and reliable estimates of IR excess. The error bars represent the range of values in the case of a uniform distribution and the standard deviation for a Gaussian distribution, as specified in Table 2.

Figure 3 shows the theoretical prediction of the ratio of IR emission in the hard state versus the soft state (i.e., $10^{0.4\Delta m_{\text{IR,pred}}}$) as a function of the inclination angle for various Lorentz factor values, assuming the disk radius and C to be the same for all ($C = 1$ and $R = 1$, i.e., $D_{\text{pr}} = \cos(i)$). As expected, we see that the IR excess is high for both very low and very high inclination values, while the intermediate inclination range shows very little IR excess for all Lorentz factors. We also plot all of the BHXBs for which IR excess and inclination angles are well constrained. It is encouraging to note that all the BHXB sources occupy the region theoretically predicted by our model.

3.3. Model Uncertainties

The uncertainty on the Doppler factor Δ_{jet} is dominated by the uncertainty related to the inclination of the source. On the other hand, the uncertainty on the projected disk area depends on the mass of the compact object, the mass of the companion star, the orbital period, and the inclination angle. The dominant source of uncertainty in calculating the expected IR flux change is the inclination angle because the projected disk area is proportional to the $2/21$ power of the sum of its component masses and the $4/21$ power of the orbital period (see Equation (1)). Hence, it is essential to use only those sources for the analysis that have a reliable estimate of the inclination. As described in Section 2, we only use inclination angles derived either from optical measurements or through radio observations, to maintain uniformity and reliability.

Since the uncertainties involved in the masses of the compact object and its companion star do not contribute much to the IR magnitude change uncertainty, this gives us the possibility of using a standard mass range for compact object and companion stars in BHXBs if these parameters are not well known for a source. For example, when we have just a lower limit for the mass of the compact object, we place a conservative upper limit of $25 M_{\odot}$ in our Bayesian analysis. We also assume a conservative lower limit of $2 M_{\odot}$ for the mass of the compact object (below which it would be a neutron star). Similarly, we place a conservative lower limit of $0.08 M_{\odot}$ on the mass of the

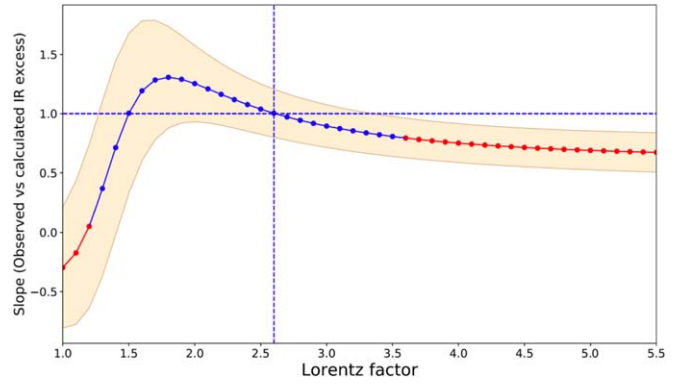


Figure 4. Best Lorentz factor values (when $C = 1$) by looking at the slopes. A slope of 1 (in the Y-axis) implies that the distribution of observed IR excess matches with the predicted one, for that particular Lorentz factor. The shaded region represents the 1σ error on the value of slope. We see that only the Lorentz factors in the range of 1.3–3.5 (shown here with blue points) are in agreement with having a slope of 1 within the errors.

companion star (below which is the brown dwarf regime). Finally, we also enforce a lower limit of 2 hr on the orbital period, since no dynamically confirmed BHXB system is known to have an orbital period of less than 2 hr.

4. Jet Lorentz Factor Estimation

We aim to constrain for the first time the jet Lorentz factors for the nine BHXBs with good data from Table 2. We will do this by modeling the observed IR magnitude change $\Delta m_{\text{IR,obs}}$ for each BHXB using the prior constraints on inclinations, component masses, and orbital periods tabulated in Table 2, along with our simple analytical model specified in Section 3.2 (namely, Equations (1), (2), and (4)).

As a first test, we initially assume a common Lorentz factor for all BHXBs, to investigate whether relativistic beaming is likely to be a realistic cause of the differing IR excess amplitudes between sources. For this, we calculate the predicted IR excess ($\Delta m_{\text{IR,pred}}$, using Equations (1), (2), and (4)) for each of these sources using different Lorentz factors and assuming the constant to be $C = 1$. In this test, we do not include XTE J1118+480, as there are two model-dependent values of observed IR excess for this source, which differ from each other by more than 2.5 mag. A preliminary way of estimating which Lorentz factor range best reproduces the observed IR excess seen in BHXBs is to just check the slope between the observed and predicted values of IR magnitude change during state transition. A slope of 1 will automatically mean that the distribution of observed IR excess matches with the calculated one for that particular Lorentz factor. As shown in Figure 4, we see that only for the Lorentz factors in the range of 1.3–3.5 are the predicted IR excesses in agreement with the observed ones. This approach suggests a Lorentz factor value of 2.6, for which the observed and predicted flux ratios are highly correlated with a slope of 1. The slope systematically deviates from 1, and the correlation becomes weaker as we move to other Lorentz factors (see Figure 4).

For the Lorentz factor of 2.6, we show the predicted versus the observed magnitude change in Figure 5. There is clearly a strong correlation (Pearson r -coefficient = 0.9, p -value = 0.001), indicating that it is very likely that the Lorentz factor plays an important role in the amplitude of the IR excess in BHXBs. For Lorentz factor = 1, i.e., nonbeamed emission, we find that there is no correlation at all (Pearson r -coefficient = -0.2 , p -value = 0.461).

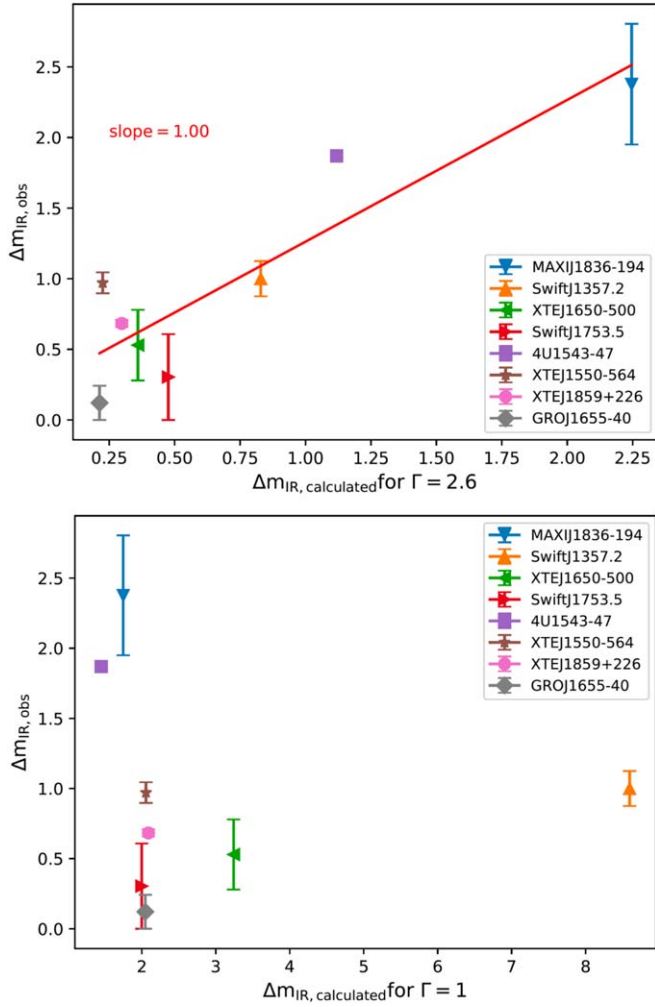


Figure 5. Top panel: predicted vs. observed NIR magnitude change when the jet switches on and/or off, assuming the best-fit Lorentz factor of 2.6. Bottom panel: no correlation is visible between the predicted observed IR magnitude change for a Lorentz factor = 1.

This strongly supports the IR emission in the hard state to be outflowing and beamed, with a likely Lorentz factor of 1.3–3.5 (when $C = 1$). But it is highly unlikely that all the BHXBs will have just one Lorentz factor. For a proper analysis, we turn to Bayesian statistics.

4.1. Hierarchical Bayesian Model

For a detailed study, we adopt a Bayesian framework in which to analyze our data. First, let us employ a subscript j to denote a specific object, with j running from 1 to 9. Then, for the j th BHXB, we have an observed datum $\Delta m_{\text{IR,obs},j}$ and five BHXB-specific model parameters i_j , $M_{\text{BH},j}$, $M_{\text{CS},j}$, $P_{\text{orb},j}$, and Γ_j . The parameter C in our model applies to all BHXBs as discussed in Section 3.2. The parameters i_j , $M_{\text{BH},j}$, $M_{\text{CS},j}$, and $P_{\text{orb},j}$ all have prior constraints, whereas the parameters Γ_j do not. We therefore assume that the parameters Γ_j are drawn from a parent distribution common to BHXBs, parameterized by a single parameter α (see later in this section). In total we have nine data points, 47 parameters, and various prior constraints.

For notational convenience, let

$$\mathbf{D} \equiv \{\Delta m_{\text{IR,obs},j}\}_{j=1}^9 \quad (5)$$

$$\theta_j = (i_j, M_{\text{BH},j}, M_{\text{CS},j}, P_{\text{orb},j}) \quad (6)$$

$$\Theta = (\theta_1, \dots, \theta_9, C) \quad (7)$$

$$\mathbf{G} = (\Gamma_1, \dots, \Gamma_9). \quad (8)$$

Using \mathcal{M} to represent the entirety of our model and its assumptions, we may write the posterior probability distribution over all of our parameters as

$$P(\Theta, \mathbf{G}, \alpha | \mathbf{D}, \mathcal{M}) \propto P(\mathbf{D} | \Theta, \mathbf{G}, \mathcal{M}) P(\Theta | \mathcal{M}) P(\mathbf{G} | \alpha, \mathcal{M}) P(\alpha | \mathcal{M}), \quad (9)$$

where the prior probability distribution for the subset of model parameters Θ is given by

$$P(\Theta | \mathcal{M}) = P(C | \mathcal{M}) \prod_{j=1}^9 [P(i_j | \mathcal{M}) P(M_{\text{BH},j} | \mathcal{M}) \times P(M_{\text{CS},j} | \mathcal{M}) P(P_{\text{orb},j} | \mathcal{M})]. \quad (10)$$

These expressions have been derived using Bayes's theorem, the definition of conditional probability, and by assuming independence of the prior probabilities.

The prior constraints (probability density functions [pdf's]) on the parameters i_j , $M_{\text{BH},j}$, $M_{\text{CS},j}$, and $P_{\text{orb},j}$ that feature in Equation (10) are listed in Table 2. If the entry for a parameter in Table 2 is given as a range, then the prior pdf for the parameter is assumed to be a uniform distribution over the range (except for inclination, where the prior pdf is assumed to be uniform in $\cos(i_j)$ over the range to satisfy isotropic orientation). If the entry for a parameter in Table 2 is given in the form $\mu \pm \sigma$, then the prior pdf for the parameter is assumed to be a Gaussian distribution with mean μ and standard deviation σ , and with hard cutoffs at 0° and 90° for i_j , 2 and 25 M_\odot for $M_{\text{BH},j}$, 0.08 M_\odot for $M_{\text{CS},j}$, and 2 hr for $P_{\text{orb},j}$ (see Section 3.3). Finally, if the entry for a parameter in Table 2 is given as a lower/upper limit, then the prior pdf for the parameter is assumed to be a uniform distribution over the range up/down to the hard cutoffs previously mentioned. The prior pdf $P(C | \mathcal{M})$ is chosen to be uniform in $\ln C$ with unrestricted range so as to limit C to strictly positive (physical) values while assuming that all orders of magnitude for C are equally likely a priori. These priors effectively serve as a regularization of the 37 model parameters in Θ in the Bayesian inference problem.

The next ingredient required in our hierarchical Bayesian model is the definition of the parent distribution for the jet Lorentz factors of BHXBs. For AGN jets, many studies find bulk Lorentz factor distributions in the form of a power law ($N(\Gamma) \propto \Gamma^\alpha$ with $\alpha < -1$; Padovani & Urry 1992; Lister & Marscher 1997; Saikia et al. 2016; see Section 5.3 for a detailed discussion). Therefore, we adopt the following parent pdf for each parameter Γ_j :

$$P(\Gamma_j | \alpha, \mathcal{M}) = \begin{cases} 0 & \text{for } \Gamma_j < 1 \\ -(\alpha + 1) \Gamma_j^\alpha & \text{for } \Gamma_j \geq 1 \end{cases} \quad (11)$$

and, assuming independence for the Γ_j , we may write

$$P(\mathbf{G} | \alpha, \mathcal{M}) = \prod_{j=1}^9 P(\Gamma_j | \alpha, \mathcal{M}). \quad (12)$$

For the (hyper)-prior pdf $P(\alpha | \mathcal{M})$, we assume a uniform distribution over the range from negative infinity to -1 .

The final ingredient required in our hierarchical Bayesian model is an expression for the likelihood function of our data

\mathbf{D} , represented as $P(\mathbf{D} | \boldsymbol{\Theta}, \mathbf{G}, \mathcal{M})$. We assume that all data points are independently observed, and we may therefore write

$$P(\mathbf{D} | \boldsymbol{\Theta}, \mathbf{G}, \mathcal{M}) = \prod_{j=1}^9 P(\Delta m_{\text{IR},\text{obs},j} | \theta_j, \Gamma_j, C, \mathcal{M}). \quad (13)$$

The individual data point likelihoods may be computed by adopting a noise model as part of our full model \mathcal{M} . We have

$$\Delta m_{\text{IR},\text{obs},j} = \Delta m_{\text{IR},\text{pred},j} + \epsilon_j, \quad (14)$$

where ϵ_j is a noise contribution and $\Delta m_{\text{IR},\text{pred},j}$ is computed from the parameters i_j , $M_{\text{BH},j}$, $M_{\text{CS},j}$, $P_{\text{orb},j}$, Γ_j , and C (using Equations (1), (2), and (4)). In Table 2, the IR excess is listed either as a range from a to b or as two numbers $a \pm b$. For a BHXB with the IR excess listed as a range, we set

$$\Delta m_{\text{IR},\text{obs},j} = \frac{1}{2}(a + b) \quad (15)$$

$$P(\epsilon_j | \mathcal{M}) = U(\epsilon_j | -(b - a)/2, (b - a)/2), \quad (16)$$

where $U(x | u, v)$ represents a uniform distribution with lower and upper limits u and v , respectively. Otherwise, we set

$$\Delta m_{\text{IR},\text{obs},j} = a \quad (17)$$

$$P(\epsilon_j | \mathcal{M}) = N(\epsilon_j | 0, b), \quad (18)$$

where $N(x | u, v)$ represents a Gaussian distribution with mean u and standard deviation v . Putting this together, we have

$$P(\Delta m_{\text{IR},\text{obs},j} | \theta_j, \Gamma_j, C, \mathcal{M}) = P(\epsilon_j | \mathcal{M}). \quad (19)$$

In the top panel of Figure 6, for each BHXB, we plot surfaces that are proportional to the prior probability density as a function of inclination i (x-axis) and observed IR excess $\Delta m_{\text{IR},\text{obs}}$ (y-axis). The surfaces are defined by the prior pdf's for the inclinations and the observed $\Delta m_{\text{IR},\text{obs}}$ values, along with the adopted noise model, that are listed in Table 2. A good model for the data \mathbf{D} should be able to reproduce the peak densities for $\Delta m_{\text{IR},\text{obs}}$ without yielding inferred inclinations that are too far away from the peaks of their corresponding prior pdf's.

The inspiration and guidance for the above development of a hierarchical Bayesian model have been taken from studying the papers by Hogg et al. (2010) and Kelly et al. (2012), although there are many examples of usage of this modeling technique in the recent astronomical literature.

4.2. Parameter Inference

We maximize the logarithm of the posterior pdf in Equation (9) over the 47 parameters in our model by using the Nelder–Mead simplex algorithm (Nelder & Mead 1965; Wright 1996) as implemented in the Python package `scipy.optimize`. This yields a maximum a posteriori (MAP) estimate of the best-fit parameters, which we report in Table 3, and some of which are plotted in Figures 6 (top panel), 7, and 8. Specifically, the best-fit parameters lead to a good fit to the data \mathbf{D} as demonstrated⁷ in the top panel of Figure 6 (where the red plus signs are the best-fit model values, while the colored surfaces are the prior pdf's). We find that the algorithm converges to the same MAP solution

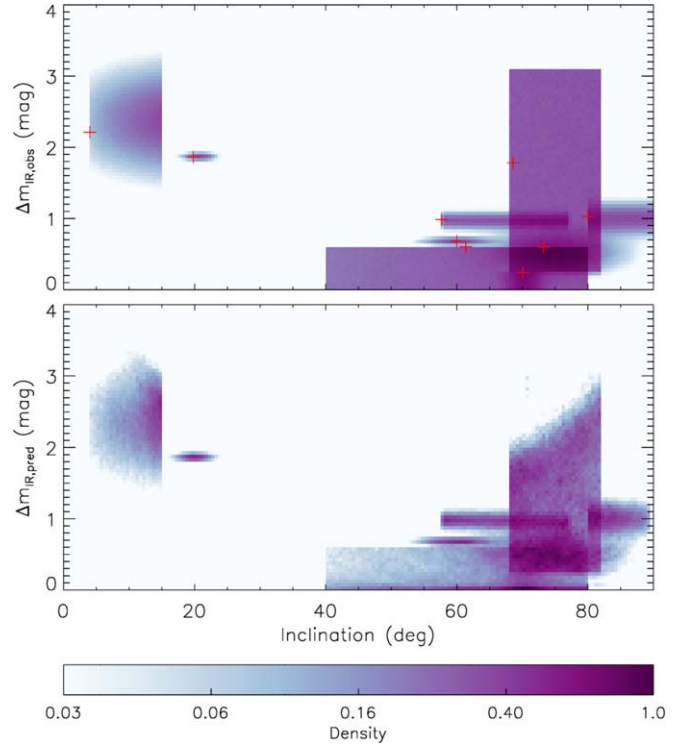


Figure 6. Top panel: plots of surfaces, for each of the nine BHXBs, that are proportional to the prior pdf as a function of the inclination i (x-axis) and observed IR excess $\Delta m_{\text{IR},\text{obs}}$ (y-axis). Red crosses show the best-fit model values for each source. The relevant probability densities for each BHXB are defined in Table 2. Bottom panel: two-dimensional histograms (normalized by peak), for each of the nine BHXBs, of posterior inferred inclination i (x-axis) and predicted IR excess $\Delta m_{\text{IR},\text{pred}}$ (y-axis) constructed using the 2×10^6 MCMC samples (see Section 4.2). Bottom: color–intensity bar (logarithmic scale) for the density surfaces in each panel.

each time so long as the initial values of the parameters that are constrained with uniform prior pdf's lie within the acceptable ranges (otherwise, the algorithm fails to converge).

We sample the posterior pdf (Equation (9)) using the Markov Chain Monte Carlo (MCMC) ensemble sampler `emcee` (Foreman-Mackey et al. 2013) with 1000 walkers initialized in a tight Gaussian ball around the MAP parameter estimates (Hogg & Foreman-Mackey 2018). Each walker executes a burn-in of 200 steps and then iterates through 50,000 subsequent steps, of which the last 2000 steps are recorded. Due to the relatively high dimensionality of the model, we found that it was necessary to set the proposal scale parameter to a nondefault value of $a = 1.15$ so as to achieve a mean acceptance fraction for each walker of ~ 0.25 . In the bottom panel of Figure 6, we use the 2×10^6 MCMC samples to plot two-dimensional histograms, for each BHXB, of posterior inferred inclination i (x-axis) and predicted IR excess $\Delta m_{\text{IR},\text{pred}}$ (y-axis). The MCMC samples clearly provide a good match to the observed IR excess $\Delta m_{\text{IR},\text{obs}}$ values within the observational noise while further constraining some of the inferred inclinations (compare the panels in Figure 6).

In Table 4, we report the median parameter values for the MCMC samples as our inferred parameter estimates with $\pm 1\sigma$ and $\pm 2\sigma$ credible regions computed using the 15.9 and 84.1 percentiles of the MCMC samples and the 2.3 and 97.7 percentiles, respectively. It should be noted that these parameter estimates, when taken together, do not represent a “best-fit” solution (see

⁷ Wherever a uniform distribution, or a hard limit, is employed in our model (i.e., in the prior pdf's and the noise model), the maximum of the posterior pdf is likely to be found on the boundary of the allowed range, unless the allowed range for a particular parameter is sufficiently large. Hence, the positioning of the red plus signs at surface boundaries in the top panel of Figure 6 is not to be unexpected.

Table 3
Best-fit MAP Parameter Estimates for the Hierarchical Bayesian Model in Section 4.1

Name	Inclination (deg)	$M_{\text{BH}} (M_{\odot})$	$M_{\text{CS}} (M_{\odot})$	$P_{\text{orb}} (\text{hr})$	Γ	$\Delta m_{\text{IR,pred}}$
XTE J1118+480	68.6	7.31	0.190	4.0784143	1.00	1.782
Swift J1357.2–0933	80.0	25.00	0.402	2.82	2.39	1.028
4U 1543–47	19.80	9.40	2.453	26.793771	2.47	1.865
XTE J1550–564	57.70	9.12	0.302	37.0088025	1.36	0.986
XTE J1650–500	73.23	4.91	2.360	7.690	2.82	0.599
GRO J1655–40	70.04	5.41	1.471	62.92580	3.88	0.240
Swift J1753.5–0127	61.37	25.00	0.250	3.240	2.74	0.600
MAXI J1836–194	4.0	14.38	0.638	4.90	1.72	2.210
XTE J1859+226	60.0	11.57	5.410	6.580	2.37	0.682
C	2.410					
α	–2.316					

Note. The two free parameters that are common to all the BHXBs, namely, the constant (C) and the index of the parent power-law distribution of jet Lorentz factors (α), are also reported at the end of the table.

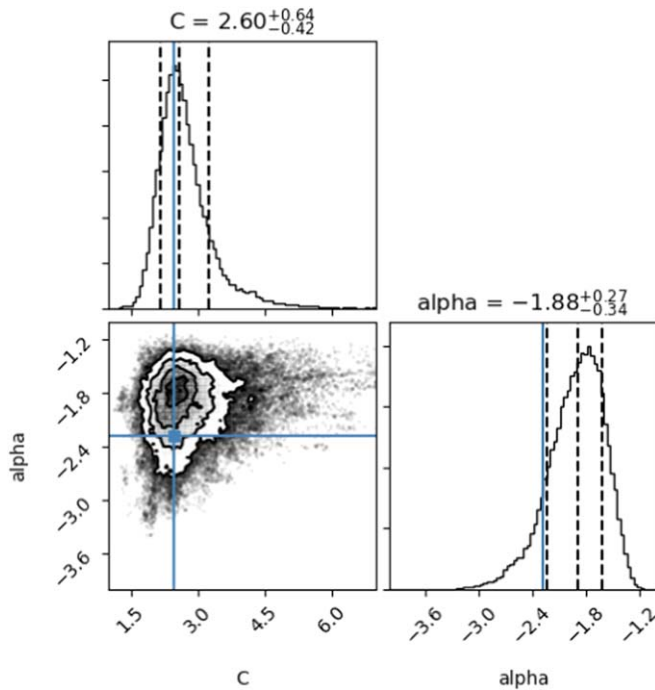


Figure 7. Top left panel: histogram of the inferred parameter C constructed using the MCMC samples. The best-fit MAP estimate is plotted with a vertical blue line, while the 15.9, 50, and 84.1 percentiles are plotted with three vertical dashed black lines. Bottom right panel: same as the top left panel, but for the inferred parameter α . Bottom left panel: two-dimensional histogram (normalized by peak) of the inferred parameters C and α , constructed using the MCMC samples. The 1σ , 2σ , and 3σ contours are also displayed. In the region outside of the 3σ contour, the individual samples are plotted. The best-fit MAP estimate for each parameter is also plotted with a blue line.

Hogg & Foreman-Mackey 2018). Our main result is that $\alpha = -1.88^{+0.27}_{-0.34}$, which characterizes the parent distribution for the jet Lorentz factors of BHXBs (see Section 5.2 for a discussion). In Figure 7, we plot one-dimensional histograms of the model parameters C and α along with a two-dimensional histogram showing their covariance. The best-fit MAP parameter estimates ($\hat{C} \approx 2.410$ and $\hat{\alpha} \approx -2.316$) are plotted with blue lines, while the 15.9, 50 and 84.1 percentiles are plotted with three vertical dashed black lines. The parameters C and α are not degenerate, which is fortunate considering their role as global parameters of our model.

The individual jet Lorentz factors Γ_j for each BHXB are also of great interest. The inferred distributions are plotted as histograms (normalized by peak) in Figure 8, with the best-fit MAP parameter estimates plotted as vertical blue lines and the 15.9, 50, and 84.1 percentiles of the MCMC samples plotted as vertical dashed black lines. The inferred parent distribution for the jet Lorentz factors of BHXBs is plotted as the red curve in each panel. The posterior distribution of the Lorentz factor for XTE J1118+480 is essentially no different from the parent distribution, and it is therefore not usefully constrained by the data in Table 2. Also, GRO J1655–40 and Swift J1753.5–0127 only have well-constrained lower limits to their jet Lorentz factors (see Table 4). However, the remaining BHXBs have useful posterior constraints on their jet Lorentz factors, especially XTE J1550–564, MAXI J1836–194, and XTE J1859+226 (see Section 5.2 for further discussion).

5. Discussion

5.1. Lorentz Factor of BHXB Jets from Literature

There is no clear consensus on the value of Lorentz factors expected in BHXB jets. Following Mirabel & Rodriguez (1994), it was suggested that BHXB jets would be significantly less relativistic than AGN jets, having $\Gamma \sim 2$. Fender & Kuulkers (2001) placed an upper limit of $\Gamma < 5$, arguing that a value higher than that would probably destroy the observed correlation between radio and X-ray peak fluxes. Furthermore, Gallo et al. (2003) used the scatter in the radio/X-ray relation of BHXB jets to constrain the Lorentz factors of compact jets to $\Gamma < 2$.

There are also studies to estimate the Lorentz factor of compact jets in a few individual BHXBs. For example, Casella et al. (2010) used IR variability of GX 339–4 to constrain the Lorentz factor of the source to be $\Gamma > 2$. Russell et al. (2015) found an unusually steep radio/X-ray correlation for MAXI J1836–194 and argued that the Lorentz factor of this source needs to vary from $\Gamma \sim 1$ at low X-ray luminosities to $\Gamma \sim 3$ –4 at high X-ray luminosities to produce the observed correlation. Tetarenko et al. (2019) studied the time lags between the X-ray and radio bands for Cygnus X-1 and found a Lorentz factor value of $2.59^{+0.79}_{-0.61}$.

On the other hand, for transient jets, Fender et al. (2004) predicted their Lorentz factors to be higher than that of compact jets, although Miller-Jones et al. (2006) did not find any

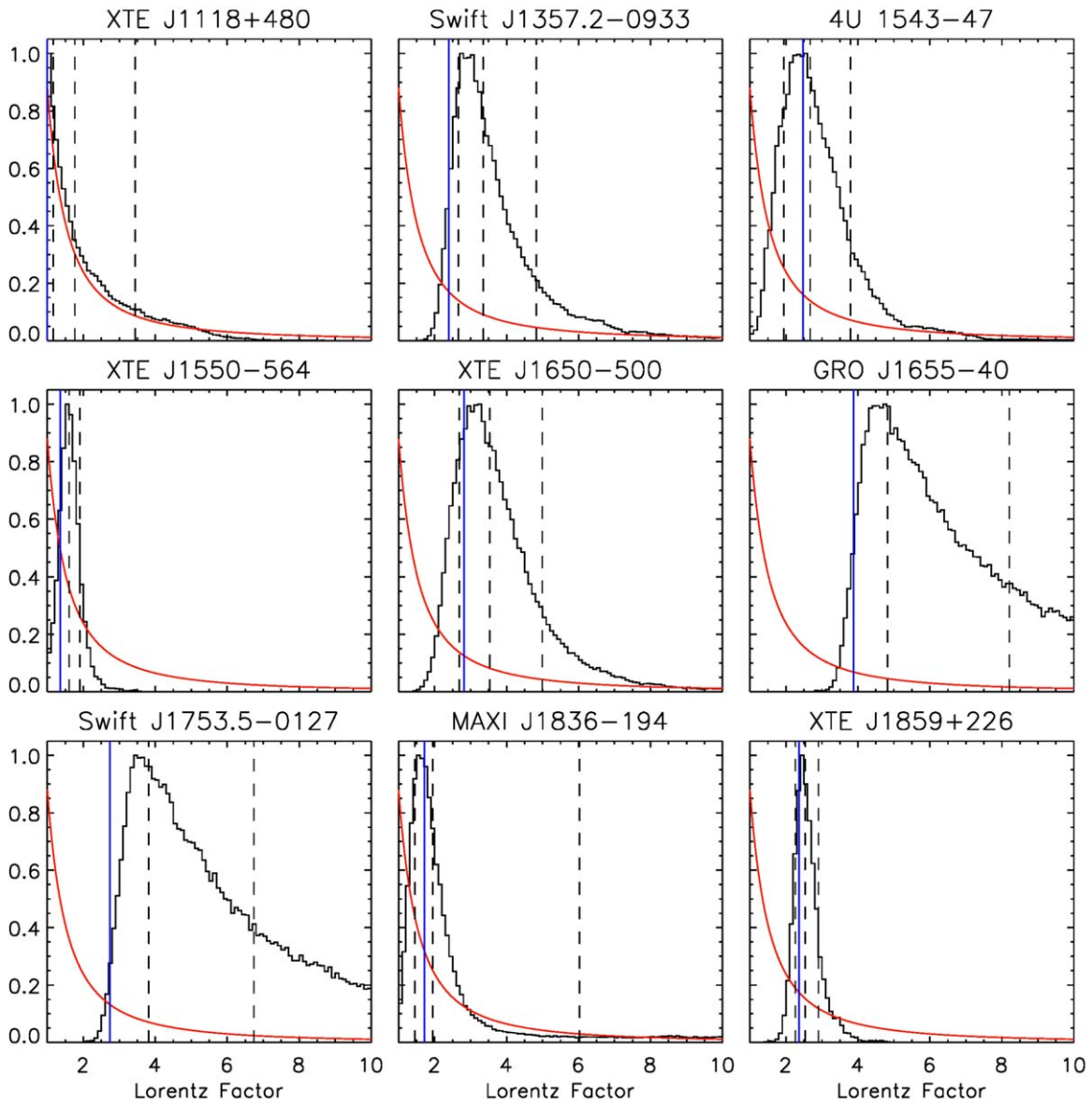


Figure 8. Histograms (normalized by peak) of the inferred jet Lorentz factors Γ_j for each BHXB, constructed using the MCMC samples. The best-fit MAP parameter estimates are plotted as vertical blue lines, and the 15.9, 50, and 84.1 percentiles are plotted as vertical dashed black lines. The red curve in each panel represents the inferred parent distribution for the jet Lorentz factors of BHXBs ($\alpha = -1.88$).

significant observational evidence to support this claim. Miller-Jones et al. (2006) collected all available data on the opening angles of “ballistic” jets in BHXBs, calculated the Lorentz factors required to produce such small opening angles via the transverse relativistic Doppler effect, and found that the derived Lorentz factors have a mean value of >10 (which is much larger than for compact jets from other studies).

But despite all these studies, it is still not clear what Lorentz factor values, or Lorentz factor distribution, can be generally expected for jets in BHXBs. We use a novel approach to attempt to answer this question for compact jets.

5.2. Implication of Our Results for Compact Jets

We find that the parent distribution of the bulk Lorentz factors for jets in BHXBs is consistent with a power law with the index $\alpha = -1.88^{+0.27}_{-0.34}$. This is very similar to their supermassive counterparts, where a bulk Lorentz factor distribution in the form

of a power law is commonly found (for example, a power law with $\alpha = -2.1 \pm 0.4$ for blazar jets, as obtained in Saikia et al. 2016).

We also estimate the individual Lorentz factors for each BHXB in our sample (see Table 4). We find that the Lorentz factors of most of the BHXB jets are quite low, for example, $1.61^{+0.29}_{-0.26}$ for XTE J1550-564, $1.94^{+0.37}_{-0.49}$ for MAXI J1836-194, and $2.53^{+0.37}_{-0.27}$ for XTE J1859+226. The Lorentz factor for Swift J1357.2-0933 was found to be $3.35^{+1.48}_{-0.69}$, that for 4U 1543-47 to be $2.67^{+1.12}_{-0.73}$, and that for XTE J1650-500 to be $3.54^{+1.45}_{-0.86}$. For two of the sources that did not have well-constrained values of observed IR excess (i.e., had either limits or model-dependent values), we can only provide limits on the bulk Lorentz factor. For example, for GRO J1655-40 and Swift J1753.5-0127 we can well constrain only the lower limits of 3.90 and 2.96, respectively. This is because the IR excess for these two objects is consistent with being zero, which allows for very high Lorentz factors because they are high-inclination sources. If more

Table 4Inferred Parameter Estimates of the Inclinations and Lorentz Factor and $\pm 1\sigma$ and $\pm 2\sigma$ Credible Regions for the Hierarchical Bayesian Model in Section 4.1

Name	Inclination (deg)	Γ
XTE J1118+480	68.3, 70.2, 75.2 , 79.7, 81.7	1.02, 1.16, 1.76 , 3.44, 5.36
Swift J1357.2–0933	80.2, 81.2, 83.8 , 87.0, 89.0	2.23, 2.66, 3.35 , 4.83, 8.25
4U 1543–47	16.67, 18.38, 19.96 , 21.51, 23.13	1.45, 1.94, 2.67 , 3.79, 6.08
XTE J1550–564	58.07, 60.32, 66.40 , 73.33, 76.57	1.11, 1.35, 1.61 , 1.90, 2.38
XTE J1650–500	62.69, 68.53, 74.44 , 79.79, 84.95	2.14, 2.68, 3.54 , 4.99, 8.80
GRO J1655–40	66.33, 68.21, 70.16 , 72.05, 73.95	3.90, 4.82, 8.21 , 25.13, 83.62
Swift J1753.5–0127	41.80, 49.78, 63.21 , 74.25, 79.12	2.96, 3.82, 6.74 , 19.25, 59.59
MAXI J1836–194	4.8, 7.8, 11.8 , 14.1, 14.9	1.17, 1.45, 1.94 , 6.00, 22.90
XTE J1859+226	53.83, 56.80, 59.94 , 62.92, 65.73	2.01, 2.26, 2.53 , 2.90, 3.58
C	1.82, 2.18, 2.60 , 3.24, 4.74	
α	–2.67, –2.22, –1.88 , –1.61, –1.40	

Note. Each entry is given as five numbers representing the 2.3, 15.9, 50 (bold), 84.1, and 97.7 percentiles of the MCMC samples. At the end, we also show the inferred values for the two free parameters that are common to all the BHXBs, namely, the constant (C) and the index of the parent power-law distribution of jet Lorentz factors (α).

(This table is available in its entirety in machine-readable form.)

accurate IR excess measurements can be made, then their Lorentz factors could be better constrained.

5.3. Comparison of BHXB versus AGN Jets

The most common way to calculate the Lorentz factor in AGN jets, particularly the relativistic jets in blazars, is by observing the apparent speed of the jet and estimating the Doppler beaming factor. The apparent speed of the jets can be calculated directly by using Very Long Baseline Interferometry (VLBI) observations (e.g., Jorstad et al. 2001; Kellermann et al. 2004; Britzen et al. 2008), but it is much more complicated to estimate the Doppler beaming factor (see Lähteenmäki and Valtaoja 1999, for a comparison of different methods). They have found that a typical radio-loud quasar has a Lorentz factor >10 , while a typical BL Lac object has a Lorentz factor >5 .

Many studies have tried to constrain the Lorentz factor distribution of the AGN population as a whole, instead of estimating the Lorentz factor for individual sources. A power-law form of Lorentz factor distribution has been seen for the most relativistic AGN jets, mainly found in blazars. Padovani & Urry (1992) found a Lorentz factor distribution in the form of $N(\Gamma) \propto \Gamma^{-2.3}$, while Lister & Marscher (1997) used a distribution of the form $N(\Gamma) \propto \Gamma^\alpha$, where $-1.5 < \alpha < -1.75$. Recently, Saikia et al. (2016) constrained a distribution of $N(\Gamma) \propto \Gamma^{-2.1 \pm 0.4}$ in the Γ range of 1–40 using the optical fundamental plane of BH activity (Saikia et al. 2015). It is interesting to note that the parent Lorentz factor distribution for BHXBs obtained from this study is quite similar to the Lorentz factor distributions expected for AGNs and follows the relation $N(\Gamma) \propto \Gamma^{-1.88^{+0.27}_{-0.34}}$.

5.4. X-Ray Flux and Lorentz Factor

Assuming that the IR excess is caused by the onset of a jet in the hard state, it is also important to check whether there is a correlation between the observed IR excess (or indirectly the Lorentz factor) and the X-ray luminosity of the source during the transition. If such a correlation exists, then it is important to normalize the IR excess of these sources by first removing the effect of having different X-ray luminosity during the transition, in order to correctly use the IR excess to constrain the Lorentz factor of these sources. To check this, we use the

average X-ray luminosity of our sample in the 2–10 keV energy band, calculated from the X-ray fluxes observed during the start and the end of the infrared transition.

We first consider the case of GX 339–4, as this source has a fair representation of many IR excesses observed during various state transitions over the years. We measured the IR excess observed for GX 339–4 in eight different state transitions (four during the transition to the soft state and another four during the transition to the hard state). We see that the IR excess measured when the source is transitioning to the hard state is always in a similar range (~ 1.5 mag change in IR). But on the other hand, the IR excess measured during the transition to the soft state varies with respect to the X-ray luminosity of the system. For smaller X-ray luminosities, the IR excess is small (~ 1.5 mag, similar to the IR excess measured during the transition to the hard state), while for higher X-ray luminosities the IR excess measured is much higher (~ 3.2 mag). Thus, we see two different ranges of IR excess for GX 339–4, but there is no single trend correlating the X-ray luminosity (2–10 keV) to the IR excess observed (see Figure 9). We find that using a larger X-ray energy range of 0.1–100 keV (for sources with available data) does not significantly change the results.

XTE J1550–564 is the only other source for which we had a measurement of IR excess during both the rise and the drop of the source. It is interesting to note that the IR excesses seen in both these transitions are remarkably similar, although the X-ray luminosities during these two transitions were different. So we cannot find a correlation between the X-ray luminosity and the observed IR excess for XTE J1550–564. Although for higher X-ray luminosity ranges we saw that GX 339–4 has a different range of IR excess, all the other BHXBs in our sample do not have such high X-ray luminosity, except XTE J1859+226. For XTE J1859+226, the inclination is $\sim 60^\circ$. As shown in Figure 1, this inclination is neither too high nor too low to have much effect on IR excess for different Lorentz factors. Hence, we find no evidence for a dependency of X-ray luminosity, except above $10^{37.5}$ erg s $^{-1}$ (2–10 keV). Therefore, we do not need to normalize the IR excess for any possible effect of having different X-ray luminosities during the transition. We note that generally at the hard-to-soft transition, the IR emission and the hard X-ray flux drop simultaneously, before the drop in the radio wavelengths (see, e.g., Figure 1 in

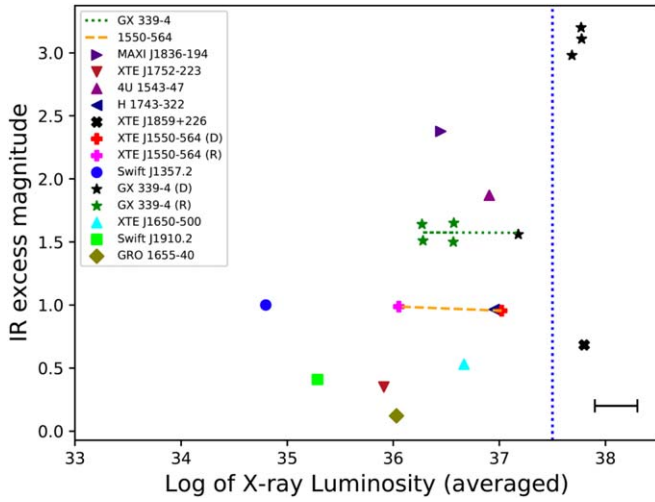


Figure 9. IR excess dependence on X-ray luminosity (2–10 keV) for XTE J1550–564, GX 339–4, and all the other BHXB sources in our sample. As seen for XTE J1550–564 (shown as plus signs, red for IR excess seen during rise (R), i.e., if the IR excess is measured during SS to HS transition, and pink during drop (D), i.e., when measured during hard-to-soft transition), we see that the same IR excess is seen in both the rise and the drop of the source. On the other hand, for GX 339–4 (shown here with green stars for rise and black stars for drop), there are two ranges of IR excess observed at different X-ray luminosity ranges. The blue dotted line is plotted to illustrate the difference at higher luminosity. A typical error bar representing the uncertainty of the X-ray luminosity, owing to the variability of X-ray flux during the infrared transition, is shown for reference in the lower right part of the plot.

Homan et al. 2005). On the other hand, at the soft-to-hard transition, the radio flux and the hard X-ray flux rise first, followed by the IR after a significant delay (~ 10 – 12 days in the case of GX 339–4; see, e.g., Corbel et al. 2013). The date range of the IR rise over this transition may not therefore correspond to the dates of the X-ray transition exactly. However, changing this date range would only serve to shift some of the data points slightly in the horizontal direction in Figure 9, which does not change the conclusions here, and the amplitude of the IR excess remains the same. As there are only two sources in our sample for which we have data on both IR drop and rise, our data are currently insufficient to test for any dependency of the IR drop or rise and the X-ray luminosity at which this occurs on other physical processes like the internal jet evolution during the transition. With more data, we could test this in a follow-up work.

It is unclear why the IR excess of GX 339–4 appears to have two populations (~ 1.5 mag and ~ 3 mag). However, if, as our model assumes, relativistic beaming is responsible for the amplitude of the IR excess, it could be suggested that the Lorentz factor increases for GX 339–4 at these very high luminosities of 10^{38} erg s $^{-1}$. This would require the inclination to be low (see below) such that the jet is pointing toward us. At these high luminosities, at the point in which the source is making a transition toward the soft state, the inner radius of the disk is moving to smaller radii and the hot flow region is shrinking (e.g., Fender & Muñoz-Darias 2016 and references therein). This may result in the Lorentz factor increasing (see Fender et al. 2004; Russell et al. 2015) and could be caused by the BH spin playing a role in boosting the jet velocity, although this is speculative. For all other X-ray luminosities (below $10^{37.5}$), we find no evidence for a relation between the Lorentz factor and the luminosity, but we do find evidence (in the only

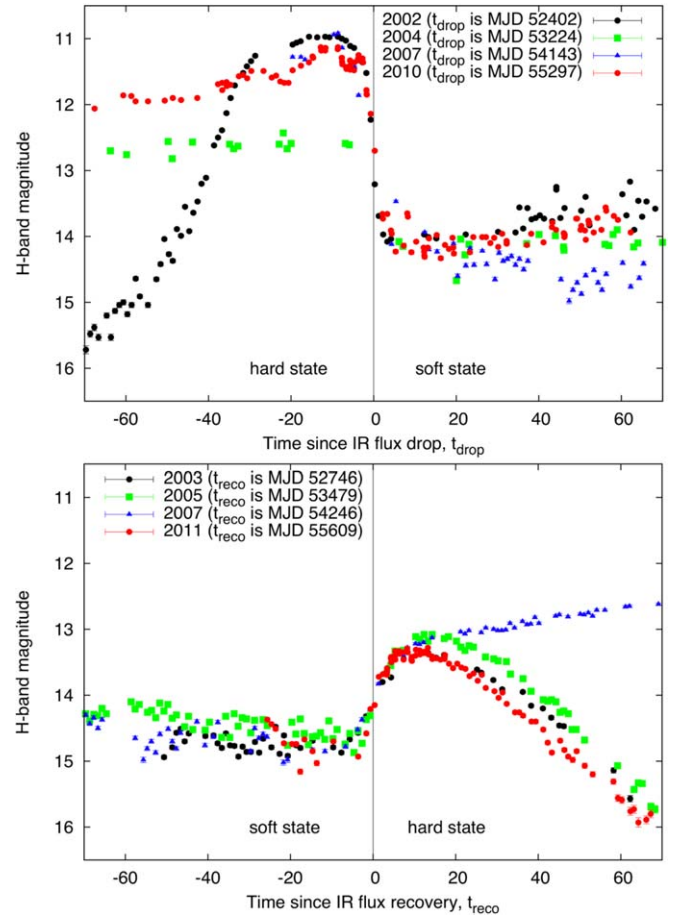


Figure 10. Overall light curves of all the times when GX 339–4 went into a transition and showed an IR excess/drop in the spectra.

two BHXBs with more than one measurement) of a constant value for the Lorentz factor at different X-ray luminosities. Hence, although both the jet flux and disk flux increase with mass accretion rate, this analysis shows that the Lorentz factor changes the jet flux, giving a boost to some and a reduction to others, compared to the disk flux. The Lorentz factor and the inclination angle appear to define how bright the jet is compared to the disk, at any given X-ray luminosity.

5.5. IR Excess and the Inclination of GX 339–4

GX 339–4 is one of the best-studied BHXBs at IR wavelengths. There are four transitions of this source that were properly covered in the IR regime (2004, 2005, 2007, and 2010), during both the rise phase and the decay phase. A combined plot of all the times when this source went into a transition and showed an IR excess/drop in the spectra is shown in Figure 10. As shown, the H -band magnitude before the transition to the hard state is almost the same for all four outbursts. Similarly, after the compact jet switches off and the source transits to the soft state, the H -band magnitude drops back to the same value for all four outbursts, irrespective of the H -band magnitude during the hard state. If we take the behavior of GX 339–4 to be typical of BHXBs, then we can say that it is better to calculate the IR magnitude change during the soft-to-hard transition, as the data seem to be more consistent compared to the flux drop during the hard-to-soft transition (this may only be an issue at very high X-ray luminosities; see Section 5.4).

The inclination of GX 339–4 is very weakly constrained. Cowley et al. (2002) make the argument that the orbital inclination has to be less than 60° from the lack of eclipses present in the optical data. Ludlam et al. (2015) argue that the inclination cannot be lower than $\sim 40^\circ$ in order to have a dynamical mass consistent with the findings of Hynes et al. (2003). Yamada et al. (2009) found a possible range of inclination of 25° – 45° at 90% confidence level. However, Wu et al. (2001) carried out optical spectroscopic observations of GX 339–4 during its high-soft and low-hard X-ray spectral states and found that the orbital inclination is about 15° if the orbital period is 14.8 hr. While Kolehmainen & Done (2010) find that inclinations $i > 45^\circ$ give better fits in the high-soft state when fitting the disk continuum to measure the spin, Shidatsu et al. (2011) analyze the iron K line with a diskline model to arrive at a best-fit inclination angle of $\sim 50^\circ$. Most recently, Heida et al. (2017) analyzed the radial velocity curve and projected rotational velocity of GX 339–4 and constrained the binary inclination to $37^\circ < i < 78^\circ$. Our analysis predicts that the inclination of GX 339–4 should be much lower than what was previously expected by many studies, as the observed IR excess of GX 339–4 is consistent with our model only if $i \lesssim 15^\circ$ (see Figure 3).

5.6. Caveats of Our Study and Errors Involved

It is important to note the caveats in our study, which could contribute to the uncertainty in the results of this paper and possibly increase the free parameters in our model. The physical parameters of our sample, including the masses of the compact object and companion star, the inclination angle of the source with respect to the line of sight and the orbital period, etc., are collected from the literature. Different methods (mainly using optical or radio observations) have been used to estimate the inclination of the sources, which is the major source of error. For the inclination obtained from optical studies, we have assumed that the jet is perpendicular to the orbital plane. Indeed, Fragos et al. (2010) predict that the majority of BHXBs have rather small ($< 10^\circ$) misalignment angles. But this might not be the case for all the sources in our sample, as there are BHXBs where the jet definitely appears to be misaligned with the binary orbit (e.g., Maccarone 2002). Furthermore, the prevalence of Type C QPOs in BHXBs suggests that if the relativistic precession model is correct (see, e.g., Stella & Vietri 1998), then the jet should be launched from the inner disk, and hence misalignments between the binary orbit and inner disk may be common.

Another variable that we have not accounted for in our model is the geometry/velocity profile of the jet. If the jet is not strictly conical but rather flared, then adiabatic expansion should kill off the low-frequency emission faster than expected, giving a more inverted spectrum. Similarly, if the jet velocity profile is not constant, but the jet accelerates on moving outward, it could beam the emission more/less at lower/higher frequencies, again affecting the spectral shape. A more inverted spectrum would imply higher jet emission relative to the disk, and vice versa for a steeper spectrum.

We also use the assumption that the whole projected disk of the BHXB contributes toward IR emission. This might not be completely true because probably only the outer part of the disk will emit in the IR regime. However, since we are calculating the “relative” IR excess for all these sources, we do not expect it to be a big issue in our analysis. Moreover, by comparing the quiescence IR magnitude of the companion star to the faintest IR magnitude of the BH system during the transition, we find

that the contribution from the companion star is much less than 10% of the total flux, except for the case of GRO 1655–40 (see Section 2.7). Hence, we neglect the IR emission coming from the companion star in our model and subtract its contribution for GRO J1655–40.

Due to the lack of enough IR monitoring of BHXBs during state transitions, while some of the IR flux changes have been calculated during the IR rise (i.e., when the source is transitioning from soft to hard state), few others were estimated during the IR decay period (i.e., when the source transitions to the soft state and the jet switches off). This could also introduce additional uncertainty in our result. Additionally, we use both *H*-band and *K*-band data to measure the IR excess. It is important to note that the amplitude of IR excess measured using *K* bands might be slightly greater than the excess measured in *H* band. Moreover, adequate IR coverage is not available for all of the sources. So while estimating the IR flux change during state transitions, the data available for some sources were severely limited and could give rise to additional uncertainties. We attempted to include such errors in the uncertainty of the observed IR excess, but better measurements are needed for future studies.

Finally, the Bayesian modeling involves making a slew of assumptions, the most important being that the Lorentz factors are drawn from a parent distribution common to BHXBs, and that this parent distribution has the form of a power law with index α as a single free (hyper-)parameter. This choice seems reasonable given that the Lorentz factors in AGN jets also appear to follow a power-law distribution. However, if this assumption is incorrect, then the results of our modeling should be taken with caution. Furthermore, we have not explored other possibilities for the parent distribution.

6. Conclusion

The NIR emission seen in BHXBs is expected to originate mainly at the outer part of the accretion disk and from the jet. An excess of IR emission is observed in many BHXBs in the hard state. We study this excess in IR emission, using a compilation of all the BHXBs in the literature for which an IR excess has been measured. Using a simple qualitative model for beaming of IR jet emission, and for the projected area of the accretion disk, we show that the amplitude of the IR fade or recovery over state transitions is expected to be very low for intermediate inclination angles (30° – 60°). The observations confirm that within this range of inclination angle, there is no BHXB with a prominent IR excess. Using the amplitude of the IR fade/recovery, the known orbital parameters, and a simple Bayesian framework, we constrain for the first time the Lorentz factor of jets in several BHXBs. Under the assumption that the Lorentz factor distribution for BHXB jets is a power law $(N\Gamma) \propto \Gamma^\alpha$, we find that $\alpha = -1.88^{+0.27}_{-0.34}$, which is remarkably similar to the index of the power law for the bulk Lorentz factor distributions of highly relativistic jets in AGNs. This work can be improved using better inclination measurements and adequate IR monitoring of more BHXBs during state transitions. We also find that the very high amplitude IR fade/recovery seen repeatedly in GX 339–4 requires a much lower inclination angle ($< \sim 15^\circ$) than previously expected by many studies. These results demonstrate how useful OIR monitoring over state transitions is for studying jet properties.

D.M.R. thanks the International Space Science Institute (ISSI) in Bern, Switzerland, for support and hospitality for the team meeting “Looking at the disk-jet coupling from different angles: inclination dependence of black hole accretion observables” in 2018 October–November. D.M.B. and D.M.R. acknowledge the support of the NYU Abu Dhabi Research Enhancement Fund under grant RE124.

ORCID iDs

James C. A. Miller-Jones  <https://orcid.org/0000-0003-3124-2814>

Maria Cristina Baglio  <https://orcid.org/0000-0003-1285-4057>

References

- Baglio, M. C., Russell, D. M., Casella, P., et al. 2018, *ApJ*, **867**, 2
- Basak, R., & Zdziarski, A. A. 2016, *MNRAS*, **458**, 2199
- Beer, M. E., & Podsiadlowski, P. 2002, *MNRAS*, **331**, 351
- Bernardini, F., Russell, D. M., Kolojnen, K. I. I., et al. 2016, *ApJ*, **826**, 149
- Blandford, R. D., & Königl, A. 1979, *ApJ*, **232**, 34
- Britzen, S., Vermeulen, R. C., Campbell, R. M., et al. 2008, *A&A*, **484**, 119
- Brocksopp, C., Fender, R. P., McCollough, M., et al. 2002, *MNRAS*, **331**, 765
- Buxton, M. M., & Bailyn, C. D. 2004, *ApJ*, **615**, 880
- Buxton, M. M., Bailyn, C. D., Capelo, H. L., et al. 2012, *AJ*, **143**, 130
- Cadolle Bel, M., Ribo, M., Rodriguez, J., et al. 2007, *ApJ*, **659**, 549
- Cadolle Bel, M., Rodriguez, J., D’Avanzo, P., et al. 2011, *A&A*, **534**, A119
- Calvelo, D. E., Vrtillek, S. D., Steeghs, D., et al. 2009, *MNRAS*, **399**, 539
- Casares, J., Rodriguez-Gil, P., Zurita, C., et al. 2012, *ATel*, **4347**, 1
- Casella, P., Maccarone, T. J., O’Brien, K., et al. 2010, *MNRAS*, **404**, L21
- Chaty, S., & Bessolaz, N. 2006, *A&A*, **455**, 639
- Chaty, S., Haswell, C. A., Malzac, J., et al. 2003, *MNRAS*, **346**, 689
- Chaty, S., Munoz Arjonilla, A. J., & Dubus, G. 2015, *A&A*, **577**, A101
- Chun, Y. Y., Dincer, T., Kalemci, E., et al. 2013, *ApJ*, **770**, 10
- Corbel, S., Aussel, H., Broderick, J. W., et al. 2013, *MNRAS*, **431**, L107
- Corbel, S., & Fender, R. P. 2002, *ApJ*, **573**, 35
- Corbel, S., Nowak, M. A., Fender, R. P., Tzioumis, A. K., & Markoff, S. 2003, *A&A*, **400**, 1007
- Coriat, M., Corbel, S., Buxton, M. M., et al. 2009, *MNRAS*, **400**, 123
- Corral-Santana, J. M., Casares, J., Munoz-Darias, T., et al. 2013, *Sci*, **339**, 1048
- Corral-Santana, J. M., Casares, J., Shahbaz, T., et al. 2011, *MNRAS*, **413**, L15
- Cowley, A. P., Schmidtke, P. C., Hutchings, J. B., & Crampton, D. 2002, *AJ*, **123**, 1741
- Curran, P. A., Chaty, S., & Zurita Heras, J. A. 2012, *A&A*, **547**, A41
- Degenaar, N., Maitra, D., Cackett, E. M., et al. 2014, *ApJ*, **784**, 122
- Dincer, T., Kalemci, E., Buxton, M. M., et al. 2012, *ApJ*, **753**, 55
- Doxsey, R., Bradt, H., Fabbiano, G., et al. 1977, *IAUC*, **3113**, 2
- Falcke, H., Körding, E., & Markoff, S. 2004, *A&A*, **414**, 895
- Fender, R., & Muñoz-Darias, T. 2016, in *Lecture Notes in Physics*, Vol. 905 ed. F. Haardt et al. (Berlin: Springer), 65
- Fender, R. P. 2003, *MNRAS*, **340**, 1353
- Fender, R. P., Belloni, T. M., & Gallo, E. 2004, *MNRAS*, **355**, 1105
- Fender, R. P., & Kuulkers, E. 2001, *MNRAS*, **324**, 923
- Foreman-Mackey, D., Hogg, D. W., Lang, D., & Goodman, J. 2013, *PASP*, **125**, 306
- Fragos, T., Tremmel, M., Rantsiou, E., & Belczynski, K. 2010, *ApJL*, **719**, 1
- Frank, J., King, A., & Raine, D. J. 2002, *Accretion Power in Astrophysics: Third Edition* (Cambridge: Cambridge Univ. Press)
- Froning, C. S., Maccarone, T. J., France, K., et al. 2014, *ApJ*, **780**, 48
- Gallo, E., Corbel, S., Fender, R. P., Maccarone, T. J., & Tzioumis, A. K. 2004, *MNRAS*, **347**, L52
- Gallo, E., Fender, R. P., & Pooley, G. G. 2003, *MNRAS*, **344**, 60
- Gallo, E., Miller-Jones, J. C. A., Russell, D. M., et al. 2014, *MNRAS*, **445**, 290
- Gandhi, P., Bachetti, M., Dhillon, V. S., et al. 2017, *NatAs*, **1**, 859
- Gandhi, P., Blain, A. W., Russell, D. M., et al. 2011, *ApJL*, **740**, L13
- Garnavich, P. M., & Quinn, J. 2000, *IAUC*, **7388**, 3
- Gelino, D. M., Balman, S., Kiziloglu, U., et al. 2006, *ApJ*, **642**, 438
- Gendreau, K., Arzoumanian, Z., Markwardt, C., et al. 2017, *ATel*, **10768**, 1
- Greene, J., Bailyn, C. D., & Orosz, J. A. 2001, *ApJ*, **554**, 1290
- Harmon, B. A., Wilson, C. A., Zhang, S. N., et al. 1995, *Natur*, **374**, 703
- Heida, M., Jonker, P. G., Torres, M. A. P., & Chiavassa, A. 2017, *ApJ*, **846**, 132
- Heinz, S., & Merloni, A. 2004, *MNRAS*, **355**, L1
- Hiemstra, B., Soleri, P., Mendez, M., et al. 2009, *MNRAS*, **394**, 2080
- Hjellming, R. M., & Rupen, M. P. 1995, *Nat*, **375**, 464
- Hogg, D. W., & Foreman-Mackey, D. 2018, *ApJSS*, **236**, 11
- Hogg, D. W., Myers, A. D., & Bovy, J. 2010, *ApJ*, **725**, 2166
- Homan, J., Buxton, M., Markoff, S., et al. 2005, *ApJ*, **624**, 295
- Homan, J., Wijnands, R., Kong, A., et al. 2006, *MNRAS*, **366**, 235
- Hynes, R. I. 2005, *ApJ*, **623**, 1026
- Hynes, R. I., Haswell, C. A., Chaty, S., Shrader, C. R., & Cui, W. 2002, *MNRAS*, **331**, 169
- Hynes, R. I., Haswell, C. A., Cui, W., et al. 2003, *MNRAS*, **345**, 292
- Hynes, R. I., Mauche, C. W., Haswell, C. A., et al. 2000, *ApJL*, **539**, L37
- Hynes, R. I., Robinson, E. L., Pearson, K. J., et al. 2006, *ApJ*, **651**, 401
- Hynes, R. I., Steeghs, D., Casares, J., Charles, P. A., & O’Brien, K. 2003, *ApJL*, **583**, L95
- Hynes, R. I., Steeghs, D., Casares, J., Charles, P. A., & O’Brien, K. 2004, *ApJ*, **609**, 317
- Jain, R. K., Bailyn, C. D., Orosz, J. A., McClintock, J. E., & Remillard, R. A. 2001, *ApJL*, **554**, L181
- Jorstad, S. G., Marscher, A. P., Lister, M. L., et al. 2005, *AJ*, **130**, 1418
- Jorstad, S. G., Marscher, A. P., Mattox, J. R., et al. 2001, *ApJS*, **134**, 18
- Kalemci, E., Begelman, M. C., Maccarone, T. J., et al. 2016, *MNRAS*, **463**, 615
- Kalemci, E., Dincer, T., Tomsick, J. A., et al. 2013, *ApJ*, **779**, 95
- Kaluzienski, L. J., & Holt, S. S. 1977, *IAUC*, **3099**, 3
- Kellermann, K. I., Lister, M. L., Homan, D. C., et al. 2004, *ApJ*, **609**, 539
- Kelly, B. C., Shetty, R., Stutz, A. M., et al. 2012, *ApJ*, **752**, 55
- Kolehmainen, M., & Done, C. 2010, *MNRAS*, **406**, 2206
- Koljonen, K. I. I., Russell, D. M., Fernandez-Ontiveros, J. A., et al. 2015, *ApJ*, **814**, 139
- Kreidberg, L., Bailyn, C., Farr, W., & Kalogera, V. 2012, *ApJ*, **757**, 36
- Krimm, H. A., Barthelmy, S. D., Baumgartner, W., et al. 2011, *ATel*, **3138**, 1
- Krimm, H. A., Barthelmy, S. D., Baumgartner, W., et al. 2012, *ATel*, **4139**, 1
- Lähteenmäki, A., & Valtaoja, E. 1999, *ApJ*, **521**, 493
- Liska, M., Hesp, C., Tchekhovskoy, A., et al. 2018, *MNRAS*, **474**, 81
- Lister, M. L., & Marscher, A. P. 1997, *ApJ*, **476**, 572
- Lloyd, C., Oksanen, A., Starr, P., Darlington, G., & Pickard, R. 2012, *ATel*, **4246**, 1
- Ludlam, R. M., Miller, J. M., & Cackett, E. M. 2015, *ApJ*, **806**, 262
- Maccarone, T. J. 2002, *MNRAS*, **336**, 1371
- Markwardt, C. B., Swank, J. H., Barthelmy, S. D., et al. 2009, *ATel*, **2258**, 1
- Mata Sanchez, D., Munoz-Darias, T., Casares, J., Corral-Santana, J. M., & Shahbaz, T. 2015, *MNRAS*, **454**, 2199
- Matilsky, T. A., Giacconi, R., Gursky, H., Kellogg, E. M., & Tananbaum, H. D. 1972, *ApJL*, **174**, L53
- McClintock, J. E., Garcia, M. R., Caldwell, N., Falco, E. E., et al. 2001, *ApJ*, **555**, 477
- Merloni, A., Heinz, S., & Matteo, T. D. 2003, *MNRAS*, **345**, 1057
- Migliari, S., Tomsick, J. A., Markoff, S., et al. 2007, *ApJ*, **670**, 610
- Miller, J. M., Fabian, A. C., Reynolds, C. S., et al. 2004, *ApJL*, **606**, L131
- Miller-Jones, J., Jonker, P. G., Ratti, E. M., et al. 2011, *MNRAS*, **415**, 306
- Miller-Jones, J. C. A., Fender, R. P., & Nakar, E. 2006, *MNRAS*, **367**, 1432
- Miller-Jones, J. C. A., Sivakoff, G. R., Altamirano, D., et al. 2012, *MNRAS*, **421**, 468
- Miller-Jones, J. C. A., Tetarenko, A. J., Sivakoff, G. R., et al. 2019, *Natur*, **569**, 374
- Mirabel, I. F., & Rodriguez, L. F. 1994, *Natur*, **371**, 46
- Motta, S. E., Casella, P., & Fender, R. 2018, *MNRAS*, **478**, 5159
- Motta, S. E., Franchini, A., Lodato, G., & Mastroserio, G. 2018, *MNRAS*, **473**, 431
- Nakahira, S., Ueda, Y., Takagi, T., et al. 2012, *ATel*, **4273**, 1
- Negoro, H., Kawase, T., Ueno, S., et al. 2017, *ATel*, **9988**, 1
- Negoro, H., Nakajima, M., Nakahira, S., et al. 2011, *ATel*, **3611**, 1
- Nelder, J. A., & Mead, R. 1965, *CompJ*, **7**, 308
- Neustroev, V. V., Veledina, A., Poutanen, J., et al. 2014, *MNRAS*, **445**, 2424
- Ogilvie, G. I., & Dubus, G. 2001, *MNRAS*, **320**, 485
- Orosz, J. A. 2003, in *IAU Symp. 212, A Massive Star Odyssey, from Main Sequence to Supernova*, ed. K. A. van der et al. (Cambridge: Cambridge Univ. Press), 365
- Orosz, J. A., Jain, R. K., Bailyn, C. D., McClintock, J. E., & Remillard, R. A. 1998, *ApJ*, **499**, 375
- Orosz, J. A., Steiner, J. F., McClintock, J. E., et al. 2011, *ApJ*, **730**, 75
- Orosz, J. A., Steiner, J. F., McClintock, J. E., et al. 2014, *ApJ*, **794**, 154
- Padovani, P., & Urry, C. M. 1992, *ApJ*, **387**, 449
- Palmer, D. M., Barthelmy, S. D., Cummings, J. R., et al. 2005, *ATel*, **546**, 1
- Plotkin, R. M., Miller-Jones, J. C. A., Jonker, P. G., et al. 2016, *ATel*, **9765**, 1

- Poutanen, J., Veledina, A., & Revnivtsev, M. G. 2014, *MNRAS*, **445**, 3987
- Rahoui, F., Coriat, M., Corbel, S., et al. 2012, *MNRAS*, **422**, 2202
- Rahoui, F., Tomsick, J. A., Coriat, M., et al. 2015, *ApJ*, **810**, 161
- Rau, A., Greiner, J., & Filgas, R. 2011, *ATel*, **3140**, 1
- Reis, R. C., Reynolds, M. T., Miller, J. M., et al. 2013, *ApJ*, **778**, 155
- Remillard, R. 2001, *IAUC*, **7707**, 1
- Remillard, R., Morgan, E., Smith, D., & Smith, E. 2000, *IAUC*, **7389**
- Russell, D. M., Curran, P. A., Munoz-Darias, T., et al. 2012, *MNRAS*, **419**, 1740
- Russell, D. M., Fender, R. P., Hynes, R. I., et al. 2006, *MNRAS*, **371**, 1334
- Russell, D. M., Maccarone, T. J., Kording, E. G., & Homan, J. 2007, *MNRAS*, **379**, 1401
- Russell, D. M., Maitra, D., Dunn, R. J. H., & Fender, R. P. 2011, *MNRAS*, **416**, 2311
- Russell, D. M., Maitra, D., Dunn, R. J. H., & Markoff, S. 2010, *MNRAS*, **405**, 1759
- Russell, D. M., Markoff, S., Casella, P., et al. 2013a, *MNRAS*, **429**, 815
- Russell, D. M., Russell, T. D., Miller-Jones, J. C. A., et al. 2013b, *ApJL*, **768**, L35
- Russell, T. D., Miller-Jones, J. C. A., Curran, P. A., et al. 2015, *MNRAS*, **450**, 1745
- Russell, T. D., Soria, R., Miller-Jones, J. C. A., et al. 2014a, *MNRAS*, **439**, 1390
- Russell, T. D., Soria, R., Motch, C., et al. 2014b, *MNRAS*, **439**, 1381
- Saikia, P., K rding, E., Coppejans, D., et al. 2018, *A&A*, **616**, A152
- Saikia, P., K rding, E., & Falcke, H. 2015, *MNRAS*, **450**, 2317
- Saikia, P., K rding, E., & Falcke, H. 2016, *MNRAS*, **461**, 297
- Sanchez-Fernandez, C., Zurita, C., Casares, J., Shahbaz, T., & Castro-Tirado, A. 2000, *IAUC*, **7506**, 3
- Shahbaz, T., Russell, D. M., Zurita, C., et al. 2013, *MNRAS*, **434**, 2696
- Shang, J.-R., Debnath, D., Chatterjee, D., et al. 2019, *ApJ*, **875**, 4
- Shaposhnikov, N., Markwardt, C., Swank, J., & Krimm, H. 2010, *ApJ*, **723**, 1817
- Shaw, A. W., Charles, P. A., Casares, J., & Santisteban, J. V. H. 2016a, *MNRAS*, **463**, 1314
- Shaw, A. W., Gandhi, P., Altamirano, D., et al. 2016b, *MNRAS*, **458**, 1636
- Shaw, A. W., Tetarenko, B. E., Dubus, G., et al. 2019, *MNRAS*, **482**, 1840
- Shidatsu, M., Done, C., & Ueda, Y. 2016, *ApJ*, **823**, 159
- Shidatsu, M., Ueda, Y., Tazaki, F., et al. 2011, *PASJ*, **63**, 785
- Smith, D. A. 1998, *IAUC*, **7008**, 1
- Steiner, J. F., McClintock, J. E., & Reid, M. J. 2012, *ApJL*, **745**, L7
- Stella, L., & Vietri, M. 1998, *ApJ*, **492**, 59
- Stiele, H., & Kong, A. K. H. 2018, *ApJ*, **868**, 1
- Tetarenko, A. J., Casella, P., Miller-Jones, J. C. A., et al. 2019, *MNRAS*, **484**, 2987
- Tetarenko, B. E., Sivakoff, G. R., Heinke, C. O., & Gladstone, J. C. 2016, *ApJS*, **222**, 15
- Tomsick, J. A., Rahoui, F., Kolehmainen, M., et al. 2015, *ApJ*, **808**, 85
- Torres, M. A. P., Callanan, P. J., Garcia, M. R., et al. 2004, *ApJ*, **612**, 1026
- Usui, R., Nakahira, S., Tomida, H., et al. 2012, *ATel*, **4140**, 1
- van der Horst, A. J., Curran, P. A., Miller-Jones, J. C. A., et al. 2013, *MNRAS*, **436**, 2625
- van Paradijs, J., & McClintock, J. E. 1994, *A&A*, **290**, 133
- Vincentelli, F. M., Casella, P., Maccarone, T. J., et al. 2018, *MNRAS*, **477**, 4524
- Wagner, R. M., Foltz, C. B., Shahbaz, T., et al. 2001, *ApJ*, **556**, 42
- Wood, A., Smith, D. A., Marshall, F. E., & Swank, J. E. 1999, *IAUC*, **7274**, 1
- Wright, M. H. 1996, in *Proc. 1995 Dundee Biennial Conf., Numerical Analysis*, ed. D. F. Griffiths & G. A. Watson (Harlow: Addison Wesley), 191
- Wu, K., Soria, R., Hunstead, R. W., & Johnston, H. M. 2001, *MNRAS*, **320**, 177
- Xu, Y., Harrison, F., Garcia, J., et al. 2018, *ApJL*, **852**, L34
- Yamada, S., Makishima, K., Uehara, Y., et al. 2009, *ApJL*, **707**, L109
- Zdziarski, A. A., Gierlinski, M., Mikolajewska, J., et al. 2004, *MNRAS*, **351**, 791
- Zurita, C., Casares, J., Shahbaz, T., et al. 2002, *MNRAS*, **333**, 791
- Zurita, C., Durant, M., Torres, M. A. P., et al. 2008, *ApJ*, **681**, 1458
- Zurita, C., Sanchez-Fernandez, C., Casares, J., et al. 2002, *MNRAS*, **334**, 999